Endophilin A1 facilitates organization of the GABAergic postsynaptic machinery to maintain excitation-inhibition balance

Xue Chen[1,2], Deng Pan[1,2], Jia-Jia Liu[1,2*] and Yanrui Yang[1*]

[1]State Key Laboratory of Molecular Developmental Biology, Institute of Genetics and Developmental Biology, Chinese Academy of Sciences, Beijing 100101, China

[2]College of Life Sciences, University of Chinese Academy of Sciences, Beijing 100039, China

*Correspondence to Yanrui Yang: yryang@genetics.ac.cn; Jia-Jia Liu: jjliu@genetics.ac.cn.

Abstract

The assembly and operation of neural circuits in the brain rely on the coordination and balance of excitatory and inhibitory activities. Inhibitory synapses are key regulators of the functional balance of neural circuits. However, due to the diversity of inhibitory presynaptic neurons, the complex composition of postsynaptic receptor subunits and the lack of typical postsynaptic dense structure, there are relatively few studies on the regulatory mechanisms for inhibitory synaptic structure and function, and insufficient understanding of the cellular and molecular abnormalities of inhibitory synapses in neurological and neuropsychiatric disorders. Here, we report a crucial role for endophilin A1 in inhibitory synapses. We show that endophilin A1 directly interacts with the inhibitory postsynaptic scaffold protein gephyrin in excitatory neurons, and promotes organization of the inhibitory postsynaptic density and synaptic recruitment/stabilization of the γ-aminobutyric acid type A receptors via its plasma membrane association and actin polymerization promoting activities. Loss of endophilin A1 by gene knockout in mouse hippocampal CA1 pyramidal cells weakens inhibitory synaptic transmission and causes imbalance in the excitatory/inhibitory function of neural circuits, leading to increased susceptibility to epilepsy. Our findings identify endophilin A1 as an iPSD component and provide new insights into the organization and stabilization of inhibitory postsynapses to maintain E/I balance as well

as the pathogenesis of epilepsy.

Key words: endophilin A1, E/I balance, epilepsy, $GABA_AR$, gephyrin, inhibitory synapse

Introduction

The excitatory and inhibitory synaptic activities of neural circuits are tightly orchestrated in the central nervous system (Sakimoto et al., 2021). The imbalance between excitatory and inhibitory neuronal activity is implicated in many neurological and neuropsychiatric diseases including schizophrenia, autism spectrum disorder and epilepsy (Canitano and Pallagrosi, 2017; Canitano and Palumbi, 2021; Foss-Feig et al., 2017; Fritschy, 2008). In the brain, in contrast to asymmetric excitatory synapses formed between axonal boutons and dendritic postsynaptic structures with thick disc-shaped PSD, inhibitory synapses are symmetric and are constituted of the presynaptic terminal from diverse interneurons and the postsynaptic plasma membrane with thin sheet-like PSD where receptor complexes are anchored (Bai et al., 2021; Favuzzi et al., 2019; Liu et al., 2020; Mody and Pearce, 2004; Tao et al., 2018). Although the formation, maturation and plasticity of both excitatory and inhibitory synapses are vitally important for neural circuit functioning, much more research efforts have been focused on the regulatory mechanisms governing excitatory synaptic structure and function. The mechanisms by which inhibitory synapses are constructed in the brain and fine-tuned in response to neural activity remain largely unexplored.

The γ-aminobutyric acid type A receptors ($GABA_ARs$), major targets of antiseizure drugs, are heteropentameric chloride channels that mediate fast synaptic transmission at inhibitory synapses in the brain (Scott and Aricescu, 2019). Several neuropathologies are characterized by alterations in $GABA_A$ receptor trafficking, synaptic E/I ratio and neuronal excitability (Sakimoto et al., 2021). At the inhibitory postsynaptic site, synaptic localization and functioning of $GABA_ARs$ requires trans-synaptic cell adhesion molecules, submembranous scaffold proteins and intracellular signaling proteins. Gephyrin is a master organizer of iPSD, which self-assembles into

planar lattices beneath the plasma membrane and anchors $GABA_A$Rs or glycine receptors (GlyRs) to the postsynaptic sites (George et al., 2021; Kasaragod and Schindelin, 2019; Kirsch et al., 1991; Tyagarajan and Fritschy, 2014). Collybistin, a membrane lipid-binding protein, functions in recruitment of gephyrin and $GABA_A$Rs to the plasma membrane by interacting with gephyrin, the synaptic adhesion molecule neuroligin-2 (NL2) and the α2 subunit of $GABA_A$Rs (Kalscheuer et al., 2009; Kins et al., 2000; Poulopoulos et al., 2009; Saiepour et al., 2010). The transmembrane protein Shisa7 binds $GABA_A$Rs and regulates their trafficking, synaptic abundance and functional properties via binding to protein(s) other than gephyrin (Han et al., 2019; Liu et al., 2020). Nevertheless, mechanisms governing the assembly, recruitment and maintenance of various inhibitory synaptic components remain largely enigmatic.

The majority of inhibitory synapses are formed on the dendritic shaft, or around the cell body of excitatory principal neurons where both actin and microtubule cytoskeletons are present underneath the plasma membrane. Through direct interaction with polymerized tubulin, gephyrin organizes the iPSD by anchoring the GlyRs and $GABA_A$Rs to the microtubule cytoskeleton (Parato and Bartolini, 2021). Notably, although small F-actin patches are observed within the dendritic shaft where the majority of inhibitory synapses are assembled (van Bommel et al., 2019), role(s) of the actin cytoskeleton in the organization and maintenance of inhibitory synapses is still unclear.

Endophilin A1 (EndoA1) is a member of the endophilin A protein family characterized by an amino (N)-terminal membrane-binding N-BIN/amphiphysin/Rvs (BAR) domain and a carboxyl (C)-terminal Src homology 3 (SH3) domain. The gene encoding endophilin A1 (*EndoA1*, gene name *sh3gl2*) is almost exclusively expressed in the brain (Ringstad et al., 1997), and has been implicated in epilepsy, schizophrenia, depression, Parkinson's disease, and Alzheimer's disease (Chang et al., 2017; Corponi et al., 2019; Germer et al., 2019; Ren et al., 2008; Yu et al., 2018a; Yu et al., 2018b). In excitatory synapses, endophilin A1 functions in synaptic vesicle recycling and autophagosome formation at the axon terminal (Bademosi et al., 2023; Milosevic et al.,

2011; Murdoch et al., 2016; Ringstad et al., 1999; Schuske et al., 2003; Soukup et al., 2016; Verstreken et al., 2003; Watanabe et al., 2018), and regulates the morphogenesis, maturation, and acute structural plasticity of dendritic spines by promoting actin polymerization via its effector protein p140Cap (Yang et al., 2021; Yang et al., 2018; Yang et al., 2015).

Previous studies reported that the double knockout (KO) mice of *EndoA1* and *EndoA2* exhibit spontaneous epileptic seizures (Milosevic et al., 2011). However, *EndoA1* depletion only causes a slight decrease in excitatory synaptic transmission in hippocampal CA1 neurons (Yang et al., 2021; Yang et al., 2018). As E/I imbalance is caused by changes in either excitatory or inhibitory activity, or both, we were prompted to investigate the biological function of endophilin A1 in the inhibitory synapses. In this study, we show that endophilin A1 interacts with gephyrin and localizes to GABAergic postsynapses. Via its membrane-binding and actin polymerization-promoting activities, endophilin A1 facilitates organization of the inhibitory postsynaptic machinery. Loss of endophilin A1 causes impairment of inhibitory synaptic transmission, E/I imbalance and aggravation of epileptic susceptibility.

Results

Ablation of endophilin A1 causes E/I imbalance and increases epilepsy susceptibility

Previous studies found that *EndoA1* and *EndoA2* double knockout (KO) mice exhibit spontaneous epileptic seizures (Milosevic et al., 2011), suggesting that endophilin A1 and A2 are involved in maintaining the E/I balance. However, another study reported that the protein levels of endophilin A1 were higher in temporal neocortex neurons of temporal lobe epilepsy (TLE) patients (Yu et al., 2018b). Moreover, in a chemical kindling mouse model of epilepsy, in which mice are chronically induced with the $GABA_AR$ antagonist pentylenetetrazole (PTZ) (Dhir, 2012), endophilin A1 was also upregulated in the hippocampus and adjacent temporal cortex, and silencing its expression in the hippocampal CA3 region reduced PTZ-induced seizure susceptibility

117 and severity (Yu et al., 2018b). To investigate the role of endophilin A1 in epilepsy, we
118 determined the impact of *EndoA1* gene ablation on chemical kindling of pan-neural
119 *EndoA1* KO mice (Yang et al., 2018) with PTZ at a sub-convulsive dose of 25 mg/kg.
120 Compared with the wild-type, PTZ-induced epileptic behaviors were significantly
121 exacerbated in *EndoA1* KO mice (Figure 1A-C and Video S1).

122 We previously found that *EndoA1* KO caused a slight decrease in the amplitude of
123 evoked excitatory postsynaptic currents (eEPSC) and a significant attenuation of long-
124 term potentiation (Yang et al., 2018). As imbalance between excitatory and inhibitory
125 signals in neuronal circuits is implicated in epilepsy, we then determined whether loss
126 of endophilin A1 in excitatory neurons affects the E/I ratio by electrophysiological
127 analysis. To this end, we eliminated the *EndoA1* gene in pyramidal neurons by
128 stereotaxic injection of adeno-associated virus (AAV) expressing CaMKIIα promoter-
129 driven Cre recombinase into the hippocampal CA1 region of $EndoA1^{fl/fl}$ mice (Figure
130 1D). Whole-cell patch clamp recording of CA1 pyramidal cells indicated that, while the
131 eEPSC and its paired-pulse ratio were not significantly changed, the evoked inhibitory
132 postsynaptic current (eIPSC), not its PPR, was decreased in the *EndoA1* KO neurons,
133 resulting in a significant increase in the E/I ratio (Figure 1E-I). Of note, neither the
134 frequency nor the amplitude of miniature EPSCs (mEPSC) or miniature IPSCs (mIPSC)
135 was altered in *EndoA1* KO neurons (Figure 1J-O). Moreover, neither fast mIPSCs
136 (perisomatic events: < 2.8 ms) nor slow mIPSCs (distal dendritic events: > 2.8 ms)
137 (Miles et al., 1996) were affected by *EndoA1* KO (Figure S1), indicating that
138 presynaptic quantal release of soma- or dendrite-targeting inhibitory synapses is normal.
139 Taken together, these data indicate that endophilin A1 in hippocampal pyramidal
140 neurons functions in inhibitory synaptic transmission to maintain E/I balance.

141

142 **Endophilin A1 is required for the formation and stabilization of inhibitory**
143 **synapses**

144 Diminished eIPSC in $EndoA1^{-/-}$ pyramidal neurons prompted us to determine the role
145 of endophilin A1 in inhibitory synapses by immunofluorescence staining of brain

146 sections from *EndoA1*$^{-/-}$ mice. Analysis of confocal microscopy images revealed that,
147 compared with the wild-type, there was a significant decrease in fluorescent signals of
148 both VGAT and gephyrin, the inhibitory pre- and post-synaptic markers, or VGLUT1
149 and PSD95, the excitatory pre- and postsynaptic markers, in all subregions of the
150 hippocampus of the *EndoA1*$^{-/-}$ mice on postnatal day 21 (P21) (Figure 2A,C,D,F, and
151 S2A,C,D,F), suggesting defects in synapse development. While a slight reduction in
152 excitatory presynaptic protein was observed, the decreases in inhibitory but not
153 excitatory postsynaptic proteins were also detected in the *EndoA1*$^{-/-}$ mice at P60 (Figure
154 2B,C,E,F, and S2B,C,E,F), indicating that the assembly and/or stabilization of
155 inhibitory postsynapses was impaired throughout brain development. Notably, gephyrin
156 signals in all layers of the different hippocampal subregions were reduced in the
157 *EndoA1*$^{-/-}$ mice (Figure S2G,H). In line with the data from immunofluorescent labeling
158 (Figure 2 and S2), decreased endogenous PSD95 or gephyrin clusters at synapses were
159 also visualized by the recombinant probes, PSD95.FingR-eGFP or mRuby2-
160 gephyrin.FingR, respectively (Bensussen et al., 2020; Gross et al., 2013), in *EndoA1*
161 KO neurons in the CA1 region at P21 (Figure S3A-D). As different types of
162 interneurons synapse with hippocampal excitatory neurons at distinct subcellular
163 compartments (soma, axon initial segment, proximal and distal dendrites) indicated by
164 the layered structures of the hippocampus (Spruston, 2008), these data suggest that
165 endophilin A1 functions in the assembly/stabilization of inhibitory synapses formed
166 between various presynaptic neurons and postsynaptic neurons.

167 Next we analyzed the $GABA_A$ receptors and found that, consistent with changes in
168 inhibitory postsynaptic marker, signals of the $GABA_AR$ γ2 subunit were decreased in
169 the hippocampi of both juvenile and adult *EndoA1*$^{-/-}$ mice (Figure 2G-I). These data
170 collectively indicate that endophilin A1 orchestrates the assembly of inhibitory
171 synapses, the architecture of inhibitory postsynapses in particular, and functioning of
172 GABAergic synapses.

173

174 **Endophilin A1 localizes to the iPSD and augments the organization of the**

175 **inhibitory postsynaptic machinery**

176 To substantiate the role of postsynaptic endophilin A1 in the assembly of inhibitory
177 synapses and exclude the impacts of presynaptic endophilin A1 and its depletion on
178 early embryonic development, we determined the effects of endophilin A1 KO on
179 inhibitory and excitatory synapses in cultured hippocampal pyramidal neurons during
180 late developmental stages. As the expression levels of $GABA_AR$ α1 are highly
181 heterogeneous in individual cultured neurons (Figure S4A), we determined the effect
182 of Cre-mediated *EndoA1* KO on surface expression of $GABA_AR$ γ2 in *EndoA1*$^{fl/fl}$
183 hippocampal neurons by immunofluorescence staining. Whilst no changes in surface
184 GluA1 was detected, the fluorescence signal intensity and number of surface $GABA_AR$
185 γ2 clusters were largely lower in dendrites of *EndoA1* KO neurons, which was rescued
186 by re-expression of endophilin A1 (Figure 3A-D). We further examined the total and
187 surface levels of synaptic proteins by immunoblotting. Biotinylation assay of surface
188 proteins revealed that, compared with wild-type, although there was no change in total
189 levels of synaptic proteins in *EndoA1* KO pyramidal neurons, the surface expression of
190 $GABA_ARs$ but not NL2 or the NR1 subunit of the NMDA-type glutamate receptor was
191 significantly reduced (Figure 3E,F). Collectively, these data indicate that postsynaptic
192 endophilin A1 enhances the surface clustering of $GABA_ARs$ and facilitates the
193 assembly of inhibitory postsynapses in pyramidal neurons.

194 Next we sought to determine the molecular function of endophilin A1 in inhibitory
195 synapses at the cellular level. By immunofluorescence staining and super-resolution
196 microscopy of hippocampal neurons in dissociated culture, we observed partial
197 colocalization of endophilin A1 with gephyrin as well as surface $GABA_AR$ γ2 in
198 dendrites of hippocampal neurons, and juxtaposition or partial colocalization of
199 endophilin A1 and VGAT puncta (Figure 3G-I and Video S2-4). We further detected the
200 localization of endophilin A1 to inhibitory synapses by co-immunostaining with both
201 pre- and post-synaptic markers (Figure. S4B and Video 5). Quantitative analysis of
202 super-resolution localization maps revealed that ~ 47 % puncta of gephyrin or Bassoon
203 were proximal to endophilin A1 (Figure. S4G, n = 14), with a mean distance between

204 endophilin A1- and gephyrin-positive pixels of ～ 120 nm, or between endophilin A1-
205 and Bassoon-positive pixels of ～ 130 nm (Figure. S4C-F). These results indicate that
206 endophilin A1 localizes to not only ePSD but also iPSD. Therefore, we speculated that
207 endophilin A1 acted as a component of iPSD. Previous studies reported that synaptic
208 $GABA_A$Rs contain the γ2 subunit along with α and β subunits (e.g., α1β2γ2) (Scott and
209 Aricescu, 2019). The γ2 subunit is essential for receptor clustering at the synapse,
210 mediated by interactions with scaffold proteins (Essrich et al., 1998). Indeed, co-
211 immunoprecipitation (coIP) of endogenous proteins in membrane fractions from mouse
212 brain lysates with antibodies against $GABA_A$R α1 detected not only the known iPSD
213 components γ2, NL2 and gephyrin, but also endophilin A1, and vice versa (Figure 3J).
214 Of note, loss of endophilin A1 caused decreases in levels of $GABA_A$R γ2 and gephyrin
215 but not NL2 in anti-$GABA_A$R α1 immunoprecipitates (Figure 3K). Further,
216 immunoblotting of synaptosome fractions revealed that the levels of $GABA_A$R γ2 and
217 gephyrin were reduced at synapses in adult *EndoA1* KO mice (Figure 3L). Together,
218 these data support that endophilin A1 functions at the iPSD to promote the assembly
219 and/or stabilization of the GABAergic postsynaptic machinery.
220

221 **Endophilin A1 directly interacts with the scaffold protein gephyrin and promotes**
222 **its clustering and localization of $GABA_A$Rs to iPSD**

223 We subsequently sought to investigate the mechanistic role of endophilin A1 in the
224 clustering of inhibitory postsynaptic proteins. To this end, we performed coIP from
225 mouse brain lysates with antibodies against endophilin A1 (Figure 4A) and analyzed
226 the immunoprecipitates by mass spectrometry. Gene Ontology (GO) analysis revealed
227 that, in addition to proteins participating in known cellular processes involving
228 endophilin A1, such as synaptic vesicle recycling, actin cytoskeleton remodeling,
229 endocytosis and long-term potentiation (Gad et al., 2000; Ringstad et al., 1999; Schuske
230 et al., 2003; Verstreken et al., 2003; Yang et al., 2021; Yang et al., 2018; Yang et al.,
231 2015), proteins related to not only glutamatergic but also dopaminergic and GABAergic
232 synapses were also identified, including gephyrin (Figure 4B and Table S1).

233 Gephyrin is the major scaffold protein which interacts with the intracellular
234 domains of $GABA_ARs$ and anchors them at the inhibitory postsynaptic membrane
235 (Essrich et al., 1998; Kneussel et al., 1999; Mukherjee et al., 2011; Tretter et al., 2008).
236 The cell adhesion molecule NL2 drives postsynaptic assembly at perisomatic inhibitory
237 synapses via interaction with gephyrin and the membrane lipid-binding protein
238 collybistin (Poulopoulos et al., 2009). We speculated that endophilin A1 functions in
239 the assembly of iPSD via interaction with the scaffold and/or intercellular adhesion
240 proteins. To determine which inhibitory synaptic protein(s) interacts with endophilin
241 A1, we performed coIP from HEK293T cells transiently expressing endophilin A1 and
242 NL2, or gephyrin, and detected interaction of endophilin A1with gephyrin but not NL2
243 (Figure 4C and 4D). Moreover, coIP from mouse brain lysates corroborated interaction
244 between endophilin A1 and gephyrin but not $GABA_AR$ α1 or γ2 (Figure 4E). Further,
245 neither endophilin A2 nor A3 interacted with gephyrin (Figure 4F).
246 Notably, although the expression levels of gephyrin were not affected by ablation
247 of *EndoA1*, its distribution in the PSD fraction was decreased (Figure 3L). In dendrites
248 of mature cultured hippocampal neurons following *EndoA1* depletion, the signal
249 intensity and number of gephyrin.FingR-eGFP clusters were also significantly
250 attenuated, with no obvious changes in PSD95.FingR-eGFP clusters (Figure S5A-D),
251 which was consistent with the reduced gephyrin but unaltered PSD95 labeled by
252 antibodies in brain slice of mature *EndoA1* KO mice (Figure 2 and S2), Moreover,
253 immunofluorescence staining revealed a decrease in the clustering of gephyrin across
254 the soma, the axon initial segment (AIS), and dendrites (Figure S5E-H). The gephyrin
255 clustering phenotype was rescued by expression of endophilin A1 but not endophilin
256 A2 or A3 (Figure 4G,H), suggesting that their functions at the inhibitory postsynapses
257 are not redundant. Conversely, overexpression of endophilin A1 caused an increase in
258 the mean signal intensity and number of gephyrin puncta in the soma and dendrites
259 (Figure 4I,J). Collectively, these data demonstrate that endophilin A1 interacts with the
260 scaffold protein gephyrin and facilitates its clustering at inhibitory postsynapses.
261 At the submembraneous postsynaptic density, gephyrin self assembles via the N-

262 terminal G and C-terminal E domains to provide scaffold for inhibitory postsynapses
263 and anchors $GABA_A$Rs to the postsynaptic sites. Consistent with the effect of *EndoA1*
264 KO on the clustering of gephyrin (Figure 4G,H) and $GABA_A$R γ2 (Figure 3A-D),
265 immunofluorescence staining and confocal microscopy analysis showed that, depletion
266 of endophilin A1 also caused a decrease in the localization of $GABA_A$R γ2 to gephyrin
267 puncta in *EndoA1* KO neurons (Figure 5A-C). Moreover, overexpression of endophilin
268 A1 also enhanced clustering of $GABA_A$R γ2 in the soma and dendrites (Figure 5D,E).
269 Together these data indicate that endophilin A1 promotes anchoring of $GABA_A$Rs to
270 the iPSD.
271 To further understand the mechanism by which endophilin A1 regulates the
272 assembly and function of inhibitory postsynapses, next we attempted domain mapping
273 of the endophilin A1-gephyrin interaction. To this end, we generated a series of
274 truncation and internal deletion mutants for endophilin A1 or gephyrin (Figure 5F). For
275 those which did not express in mammalian cells, we determined their interaction with
276 gephyrin by in vitro binding assays with recombinant proteins. None of the truncation
277 or internal deletion mutants lost the ability to bind to gephyrin, and deletion of neither
278 the BAR nor the SH3 domain weakened the binding (Figure 5G,H), suggesting that
279 they are involved in the interaction with gephyrin. Pull-down assay showed both G and
280 E domains but not C domain of gephyrin were involved in the interaction with
281 endophilin A1 (Figure 5I). Indeed, the decreases in clustering of either gephyrin or
282 $GABA_A$R γ2 in *EndoA1* KO neurons were not rescued by expression of endophilin A1
283 fragments (Figure 5J-M), indicating that all functional domains of endophilin A1 are
284 required for the assembly of the GABAergic postsynaptic machinery.
285
286 **Actin polymerization is required for stabilization of inhibitory postsynapses**
287 Endophilin A1 functions in the morphogenesis and structural plasticity of dendritic
288 spines by promoting actin polymerization underneath the plasma membrane (Yang et
289 al., 2021; Yang et al., 2018; Yang et al., 2015). Of note, previous studies reported
290 controversial results about the role of the actin and microtubule cytoskeleton in
291 gephyrin clustering (Allison et al., 2000; Charrier et al., 2006; Kirsch and Betz, 1995).

292 To further investigate the mechanism underlying endophilin A1-mediated assembly of
293 inhibitory postsynapses, we asked whether actin polymerization contributes to the
294 stabilization of iPSD and $GABA_AR$ clustering in dendrites. Consistent with previous
295 studies (van Bommel et al., 2019), we observed large patches of F-actin labeled by
296 LifeAct-mCherry in spines and small puncta in dendritic shafts that exhibited partial
297 colocalization with or adjoined gephyrin in cultured hippocampal neurons by super-
298 resolution microscopy (Figure S6A and Video S6). We then determined the impact of
299 F-actin depolymerization on gephyrin-labeled iPSD and γ2-containing $GABA_ARs$ in
300 cultured hippocampal neurons. Treatment of mature neurons with nocodazole, a
301 microtubule depolymerizing reagent, for one hour (short-term) or two hours (long-term),
302 caused decreases in the number of both PSD95 and gephyrin puncta (Figure 6A-D),
303 which was in good agreement with previous findings that microtubule dynamics
304 regulates the spatial organization of both excitatory and inhibitory postsynaptic
305 structures (Gu et al., 2008; Jaworski et al., 2009; Kirsch and Betz, 1995; Kirsch et al.,
306 1991). Short-term or long-term incubation with latrunculin A, which disrupts actin
307 polymerization, also caused decreases in the number of both ePSD and iPSD puncta
308 (Figure 6A-D), indicating that actin polymerization also contributes to the stabilization
309 of the iPSD. We then tested the effect of actin depolymerization on $GABA_AR$ clustering
310 and found that, long-term but not short-term latrunculin A application caused a
311 reduction in the number of $GABA_AR$ γ2 puncta in dendrites (Figure 6E-H), this finding
312 supported the observation that the decrease in gephyrin cluster preceded the reduction
313 in $GABA_AR$ γ2 receptor cluster following latrunculin A treatment (Figure 6I). In
314 addition, colocalization analysis revealed less recruitment of γ2 to gephyrin puncta even
315 after short-term drug application, without changes in γ2 clustering (Figure 6J,K).
316 Together, these data demonstrate that actin polymerization is essential for the
317 stabilization of iPSD and anchoring of $GABA_ARs$ to the postsynaptic sites.
318

319 **Both the membrane-binding and p140Cap-binding capacities of endophilin A1 are**
320 **indispensable for its function at the inhibitory postsynapses**

321 At the excitatory synapse, the plasma membrane-associated endophilin A1 regulates the
322 morphogenesis, maturation and structural plasticity of dendritic spines by promoting
323 branched actin polymerization underneath the postsynaptic membrane via its
324 interaction with the cytoskeleton regulator p140Cap (Yang et al., 2021; Yang et al., 2018;
325 Yang et al., 2015). Having established the requirement for both endophilin A1 and the
326 actin cytoskeleton in the assembly and stabilization of the inhibitory postsynaptic
327 structure, we speculated that regulation of inhibitory postsynapse assembly by
328 endophilin A1 necessitated its plasma membrane-binding and actin polymerization-
329 promoting activities. Silencing p140Cap expression in postsynaptic CA1 pyramidal
330 cells by shRNA-mediated knockdown caused decreases in the clustering of gephyrin
331 puncta in dendrites, which was restored by overexpression of p140Cap (Figure S6B, C),
332 suggesting that p140Cap-mediated actin polymerization is required for the assembly of
333 iPSD in postsynaptic neurons. However, compared with mere depletion of endophilin
334 A1, p140Cap knockdown did not further attenuate the clustering of gephyrin in *EndoA1*
335 KO neurons (Figure S6D, E). Moreover, overexpression of p140Cap did not rescue the
336 iPSD phenotype in *EndoA1* KO neurons (Figure 7A,B), suggesting that p140Cap-
337 enhanced actin polymerization promotes the organization of iPSD through endophilin
338 A1-mediated pathway. Indeed, overexpression of neither the membrane-binding
339 deficient (KKK-EEE) nor the p140Cap-binding deficient (Y343A) mutant of
340 endophilin A1 (Yang et al., 2021) could rescue the iPSD defect (Figure 7A,B).
341 Consistently, neither p140Cap nor the endophilin A1 loss-of-function mutants could
342 rescue the $GABA_AR$ γ2 clustering phenotype in *EndoA1* KO neurons (Figure 7C,D).
343 Collectively, these data indicate that both plasma membrane association and actin
344 polymerization-promoting activities are required for endophilin A1 to promote the
345 assembly of the inhibitory postsynaptic machinery.

346 Next, we determined the mechanistic role of endophilin A1 in vivo by rescuing the
347 epilepsy susceptibility caused by *EndoA1* KO. Indeed, when AAVs expressing the Cre
348 recombinase and endophilin A1 were co-injected into the hippocampal CA1 region of
349 $EndoA1^{fl/fl}$ mice, only the wild-type but not the membrane-binding or p140Cap-binding

deficient mutant of endophilin A1 rescued the early onset and severity of PTZ-induced seizures (Figure 7E,F and Video S7). Consistently, electrophysiological recording in acute brain slices indicated that only wild-type endophilin A1 but not the mutants restored the amplitude of eIPSC and E/I balance in *EndoA1* KO neurons (Figure 7G-K). All together, these data indicate that endophilin A1 contributes to the structure and function of inhibitory synapses by promoting the submembrane assembly of iPSD and synaptic localization of the $GABA_A$Rs, thereby maintaining the balance of excitatory and inhibitory activities in neural circuits (Figure 8).

Discussion

Although collybistin is implicated in plasma membrane recruitment and clustering of gephyrin and $GABA_A$R α2 (Saiepour et al., 2010), studies of collybistin KO mice showed that the $GABA_A$R α3 subunit promotes gephyrin-mediated formation of inhibitory synapses in the absence of collybistin (Wagner et al., 2021), raising the possibility that formation of a subset of GABAergic synapses requires gephyrin-interacting membrane-associated proteins other than collybistin. In the present study, we identify endophilin A1 as a novel binding partner for gephyrin and demonstrate that it promotes the assembly of inhibitory synapses and clustering of $GABA_A$Rs at the iPSD. Loss of endophilin A1 activity causes impairment of inhibitory synaptic transmission in neuronal circuits and increases susceptibility to seizures. In the central nervous system, inhibitory interneurons are highly diverse in morphologies, molecular profiles and physiological functions. Presynaptic terminals from different types of interneurons target distinct subcellular compartments in postsynaptic pyramidal neurons where $GABA_A$ receptors of specific subunit compositions are located. Parvalbumin-expressing (PV+) interneurons usually contact the soma and proximal dendrites, whereas somatostatin-expressing (SST+) interneurons mainly innervate the dendrites of pyramidal cells (Klausberger and Somogyi, 2008). Although different inhibitory synapses localized in different subcellular compartments of postsynaptic neurons have distinct properties and express a diversity of synaptic proteins, gephyrin

379 remains a core postsynaptic component (Favuzzi et al., 2019). Our study revealed that
380 endophilin A1 promotes the clustering of gephyrin in all subcellular compartments of
381 pyramidal neurons, indicating that endophilin A1 functions in the organization of
382 inhibitory postsynapses innervated by various presynaptic interneurons.

383 Among the endophilin A proteins, endophilin A1 is the most abundant in the brain
384 (Milosevic et al., 2011). Although they have redundant roles in physiological or
385 pathological functions (Milosevic et al., 2011), endophilin A1, but not A2 or A3,
386 promotes spine morphogenesis and excitatory postsynaptic organization (Yang et al.,
387 2018; Yang et al., 2015; Milosevic et al., 2011). Here, we uncover a previously
388 unanticipated role for endophilin A1 at GABAergic synapses. By deleting endophilin
389 As in specific neuron subtypes, we found that endophilin A1 regulates GABAergic
390 postsynaptic compartments. Endophilin A1, rather than A2 or A3, interacts with
391 gephyrin and modulates the inhibitory postsynaptic machinery. Although endophilin A1
392 might function redundantly with other endophilin As in synaptic vesicle recycling at
393 the presynaptic site, it participates in the organization or reorganization of postsynaptic
394 structures through specific binding to postsynaptic proteins, a function that cannot be
395 fully replaced by other endophilin As at both excitatory and inhibitory postsynapses.

396 The membrane lipid-binding protein collybistin interacts with the trans-synaptic
397 cell adhesion molecule NL-2 to recruit gephyrin and $GABA_AR$ α2 to the postsynaptic
398 membrane (Kalscheuer et al., 2009; Kins et al., 2000; Poulopoulos et al., 2009; Saiepour
399 et al., 2010). Adamtsl3 secreted from presynapses binds to the transmembrane protein
400 DCC (Deleted in Colorectal Cancer) and controls its synaptic localization, which is
401 required for the maintenance of GABAergic synapses in the adult brain (Cramer et al.,
402 2023). Anchoring of the α5 subunit of $GABA_AR$ to the actin cytoskeleton through
403 radixin, an actin-binding protein, facilitates its clustering (Loebrich et al., 2006). These
404 findings underscore the necessity for investigation of mechanism(s) regulating the
405 plasma membrane-iPSD-actin cytoskeleton interaction. As membrane-binding and
406 actin polymerization-promoting activities of endophilin A1 are both required for its
407 function in enhancing iPSD formation and γ2–containing $GABA_AR$ clustering to iPSD,

408 we propose that membrane-bound endophilin A1 promotes postsynaptic assembly by
409 coordinating the plasma membrane tethering of the postsynaptic protein complex and
410 its stabilization with the actin cytomatrix (Figure 8). In contrast, clustering of β2/3
411 subunit-containing $GABA_A$Rs is independent of the actin or microtubule cytoskeleton
412 in hippocampal neurons (Allison et al., 2000; Kasaragod et al., 2022). Given that
413 synaptic and extrasynaptic $GABA_A$Rs are composed of distinct subunits (Kasaragod et
414 al., 2022; Koh et al., 2023), these findings indicate that the actin cytoskeleton plays
415 distinct roles in the clustering and possibly dynamic changes in the subunit composition
416 and subcompartmental localization of different types of $GABA_A$Rs. Of note, the
417 subcellular distribution of gephyrin, which has a tubulin-binding motif, is not affected
418 by depolymerization of F-actin or microtubule (Allison et al., 2000). Overall, the
419 discrepancy in data about the involvement of the actin cytoskeleton in inhibitory
420 synapses may be due to differences in drug concentration, treatment time, receptor
421 subtypes and neuronal cell types (Mody and Pearce, 2004; Sexton et al., 2021). In the
422 present study, the impaired clustering of gephyrin and $GABA_A$ γ2 by F-actin
423 depolymerization underscores the essential role of F-actin in the assembly and
424 stabilization of the inhibitory postsynaptic machinery. Membrane-bound endophilin A1
425 promotes F-actin polymerization beneath the plasma membrane through its interaction
426 with p140Cap, an F-actin regulatory protein, thereby facilitating and/or stabilizing the
427 clustering of gephyrin and γ2-containing $GABA_A$ receptors at postsynapses.

428 The number of synaptic $GABA_A$ receptors is subject to alterations not only during
429 development and neuronal plasticity but also during pathological processes such as
430 epilepsy (Nusser et al., 1998). Synaptic $GABA_A$ receptors are recruited directly from
431 extrasynaptic pools following exocytosis, and their endocytosis occurs exclusively at
432 extrasynaptic sites (Bogdanov et al., 2006). Therefore, lateral diffusion of $GABA_A$Rs
433 between synaptic and extrasynaptic sites and their iPSD anchoring are very important
434 for their synaptic distribution (Thomas et al., 2005). In good agreement with the finding
435 that $GABA_A$Rs stabilization at synapses depends on gephyrin clustering (Jacob et al.,
436 2005), we found that decreases in gephyrin clustering precedes the reduction in surface

437 $GABA_A$Rs following F-actin depolymerization (Figure 6). As the core scaffold protein
438 in iPSD, gephyrin is highly enriched at the inhibitory postsynaptic sites and drives the
439 formation of iPSD sheets via phase separation (Bai et al., 2021). As binding of gephyrin
440 by its partner proteins inhibits the iPSD condensate formation via autoinhibition of the
441 multivalent interactions between its E domain and $GABA_A$Rs (Bai et al., 2021;
442 Hoffmann and Milovanovic, 2021; Liu et al., 2020), it is conceivable that endophilin
443 A1 binding not only tethers the scaffold protein to the plasma membrane, but also
444 releases it from the autoinhibitory conformation to facilitate the phase separation of the
445 gephyrin-receptor complexes. Whether the activity of endophilin A1 is regulated by
446 neuronal activity to participate in the structural and functional remodeling of iPSD
447 awaits further investigation.

448 At the presynaptic site of excitatory synapses, endophilin A1 functions in synaptic
449 vesicle recycling by recruiting the clathrin-uncoating factor synaptojanin (Milosevic et
450 al., 2011; Schuske et al., 2003; Verstreken et al., 2003). At the excitatory postsynapses,
451 plasma membrane-associated endophilin A1 facilitates the morphogenesis, stabilization,
452 maturation and plasticity of dendritic spines by promoting actin polymerization via its
453 interaction with p140Cap (Yang et al., 2021; Yang et al., 2018; Yang et al., 2015). In
454 this study, we demonstrate that endophilin A1 functions upstream of p140Cap in not
455 only excitatory but also inhibitory postsynapses of excitatory neurons. Intriguingly,
456 recent studies reported that p140Cap is present in the inhibitory presynaptic
457 compartment and regulates GABAergic synaptogenesis and neurotransmission (Russo
458 et al., 2019), raising the possibility that endophilin A1 and p140Cap also coordinate to
459 regulate the organization and activity of GABAergic synapses at the inhibitory
460 presynaptic site. Remodeling of inhibitory synapses and dendritic spines are spatially
461 clustered by sensory inputs in the central nervous system (Chen et al., 2012). Notably,
462 the turnover of inhibitory synapses outpace that of excitatory synapses (Chen et al.,
463 2012). Therefore, it is conceivable that deficits in inhibitory synapses are much more
464 severe in *EndoA1* KO mice, leading to perturbation of the E/I balance and increased
465 epileptic vulnerability.

Materials and Methods

Ethics statement

All animal experiments were approved by and performed in accordance with the guidelines of the Animal Care and Use Committee of Institute of Genetics and Developmental Biology, Chinese Academy of Sciences (Approval code: AP2022008). All animals were housed in standard mouse cages at 22-24°C on a 12 h light/dark cycle with access to food and water freely.

Animals

Generation of *EndoA1*$^{fl/fl}$ and *EndoA1*$^{-/-}$ (KO first) mice on the C57BL/6J background were as previously described. *EndoA1*$^{+/+}$ and *EndoA1*$^{-/-}$ mice were bred as littermates from heterozygous breeders. Genotyping of mouse lines was performed by genomic PCR of tail prep DNA from offspring with the following primer pairs: loxPF/loxPR: 5'-CAAGGACTCCCAGAGACCTAGCATC-3' and 5'-GAGATGGCGCAACGCAATTAAT-3' (A PCR product of 375 base pairs in *EndoA1* KO first mice but none in wild-type mice). zptF/zptR: 5'-gtaagcggctctagcgcatgttct-3' and 5'-GCAGGGGCATGTAGGTGGCTCAAC-3' (A PCR product of 466 base pairs in wild-type mice, none in *EndoA1*$^{-/-}$ mice, and of 627 base pairs in *EndoA1*$^{fl/fl}$ mice).

Constructs and viruses

pCMV-Tag2B-EndoA1, pCMV-Tag2B-p140Cap, pCMV-Tag2B-EndoA1 Y343A, pCMV-Tag2B-EndoA1 KKK-EEE, pCMV-Tag2B-EndoA1 (aa172-352), pGEX-4T-1-SH3 (aa295-352), pET-28a (+)-EndoA1 and LifeAct-mCherry constructs were described previously (Yang et al., 2021; Yang et al., 2015). pAOV-CAMKIIα-mCherry-2A-3FLAG were purchased from OBiO Technology (Shanghai) Corp. Ltd., (Shanghai, China). pNICE-NL2(-) was a gift from Peter Scheiffele (Addgene plasmid # 15246) (Chih et al., 2006). pCR3-FLAG-Gephyrin P1 was a gift from Shiva Tyagarajan (Addgene plasmid # 68816) (Tyagarajan et al., 2013). pCAG_PSD95.FingR-eGFP-

495 CCR5TC and pCAG_GPN.FingR-eGFP-CCR5TC were gifts from Don Arnold
496 (Addgene plasmid # 46295 & #46296) (Gross et al., 2013). The pCMV-Tag3B-GPN
497 construct was generated by cloning gephyrin cDNA amplified from pCR3-FLAG-
498 gephyrin into pCMV-Tag3B (Clontech Laboratories, Inc.). The pGEX-4T-1 EndoA1
499 ΔBAR (Δaa6-242) and pGEX-4T-1 EndoA1 ΔSH3 (Δaa1-352) constructs were
500 generated by cloning fragments amplified from pCMV-Tag2B-EndoA1 into pGEX-4T-
501 1. The pGEX-4T-1 GPN G (aa15-169), pGEX-4T-1 GPN C (aa170-326) and pGEX-
502 4T-1 GPN E (aa327-733) constructs were generated by PCR amplification from full-
503 length constructs and subcloned into pGEX-4T-1. All constructs were verified by DNA
504 sequencing. Viral particles of adeno-associated virus (AAV) carrying mCherry, EGFP,
505 the Cre recombinase, EndoA1 WT or mutants were purchased from OBiO Technology
506 (Shanghai) Corp. Ltd., (Shanghai, China). Viral particles of rAAV-EF1a-PSD95.FingR-
507 eGFP-CCR5TC and rAAV-EF1a-mRuby2-Gephyrin.FingR-IL2RGTC (Bensussen et
508 al., 2020) were purchased from brain case Corp. Ltd., (Shenzhen, China).
509
510 **Antibodies**
511 The following antibodies were obtained from commercial sources: rabbit anti-
512 endophilin A1 (159 002, Synaptic Systems GmbH, Germany), mouse anti-Gephyrin
513 (147 111, Synaptic Systems), guinea pig anti-gephyrin (147 318, Synaptic Systems),
514 mouse anti-neuroligin 2 (129 511, Synaptic Systems), mouse anti-GluA1 (MAB2263,
515 Millipore), rabbit anti-$GABA_AR$ α1 (06-868, Millipore Sigma), rabbit anti-$GABA_AR$
516 γ2 (224 003, Synaptic Systems), mouse anti-SYP (D-4) (sc-17750, Santa Cruz), rabbit
517 anti-FLAG (F3165, Sigma-Aldrich), rabbit and mouse anti-RFP which recognizes
518 DsRed, mCherry and mRuby2 (PM005 and M165-3, Medical & Biological
519 Laboratories, Naka-ku Nagoya, Japan); mouse anti-α-tubulin (T9026, Sigma-Aldrich),
520 mouse anti-PSD95 (610495, BD Biosciences, San Diego, CA) and mouse anti-GST
521 (M071-3, MBL) for western blotting (WB) and rabbit anti-VGAT (131 004, Synaptic
522 Systems), mouse anti-PSD95 (75-028, NeuroMab, Davis, CA), guinea pig anti-Ankyrin
523 G (386 004, Synaptic Systems), guinea pig anti $GABA_AR$ γ2 (224 004, Synaptic

524 Systems) and mouse anti-Bassoon (sc-58509, Santa Cruz) for immunofluorescence
525 staining; Rabbit anti-p140Cap was described previously (Yang et al., 2015). Alexa
526 Fluor dye-conjugated secondary antibodies for immunofluorescence staining were from
527 Molecular Probes (Invitrogen, Carlsbad, CA, USA).
528
529 **Pentylenetetrazole (PTZ)-kindling and Seizure Behavior Scoring**
530 To evaluate seizure susceptibility, 8-10-week-old male and female *EndoA1*$^{+/+}$ or
531 *EndoA1*$^{-/-}$ littermates or *EndoA1*$^{fl/fl}$ littermates were intraperitoneally administered with
532 PTZ (25 mg/kg; K0250, Sigma-Aldrich) or saline (control) for 8-12 days, and the
533 resulting seizure behaviors were video-recorded for the next 30 min. Seizure
534 susceptibility was measured blindly by rating seizures on a scale of 0 to 7 as follows
535 (Van Erum et al., 2019): no abnormal behavior (0), reduced motility and prostate
536 position (1), facial jerking (Schulz et al.), neck ierks (Huo et al.), clonic seizure (sitting)
537 (4), clonic, tonic-clonic seizure (lving on belly) (5), clonic, tonic-clonic seizure (lving
538 on side) and wild jumping (6), tonic extension, possibly leading to respiratory arrest
539 and death (7).
540
541 **Stereotaxic injection**
542 For virus injection, 8-9-week-old naive male and female littermates were anesthetized
543 and stereotactically injected with viral particles in the hippocampal CA1 region as
544 described (Yang et al., 2018). Briefly, mice were weighed and anesthetized with
545 isoflurane (2% 2,2,2-tribromoethanol, Sigma), and secured in a stereotaxic apparatus.
546 The scalp of mouse was cut along the midline between the ears after sterilized with
547 iodophors and 75% (vol/vol) alcohol. Holes for inserting needle were drilled in the
548 bilateral skull. Viral particles carrying pAOV-CAMKIIα-MCS-mCherry-3FLAG or
549 pAOV-CAMKIIα-mCherry-2A-Cre and pAAV-CaMKIIα-EGFP-2A-MCS-3FLAG or
550 pAAV-CaMKIIα-EGFP-2A-MCS-3FLAG-EndoA1 WT or mutants (1.2 μL, 2.0× 10^{12}
551 viral genomes/mL) (OBiO Technology Corp., Ltd) were injected bilaterally into the
552 hippocampal CA1 regions using the following coordinates relative to bregma: 2.0 mm

553 posterior, 1.8 mm lateral, and 1.4 mm ventral at a rate of 0.125 μL/min using a
554 microinjection system (World Precision Instruments). The needle was kept in place for
555 2 min before withdrawal, and the skin was sutured with surgical line. The virus-injected
556 mice were tested for behavior two weeks later.
557
558 **Immunofluorescence staining of brain sections**
559 Male and female littermates (P21 or P60) were anesthetized and immediately perfused,
560 brains were dissected out, fixed overnight in 4% (vol/vol) paraformaldehyde, incubated
561 overnight with 30% sucrose in phosphate-buffered saline (PBS), and then sliced into 30
562 μm-thick coronal sections using a cryotome (Model CM-1950; Leica Biosystems). For
563 immunostaining of brain sections, floating 30 μm-thick slices were rinsed with PBS and
564 permeabilized in 0.4% Triton X-100 in 0.01M PBS for 30 min. Cyrosections were
565 blocked with 2% BSA in PBS containing 0.4% Triton X-100 for 2 h at room temperature
566 (RT), then incubated with primary antibodies overnight at 4 °C. Secondary antibodies
567 conjugated with Alexa Fluor 488 or 555 were used for detection. Sections were then
568 incubated with DAPI (Roche, Grenzach-Wyhlen, Germany) for nuclear staining for 3
569 min at RT. Following rinsing, cyrosections were mounted on gelatin-coated slides and
570 covered with coverslip with mounting medium. Confocal images were collected using
571 the Spectral Imaging Confocal Microscope Digital Eclipse A1Si (Nikon, Tokyo, Japan)
572 with a 40× Plan Fluo (NA 1.30) oil objective (Yang et al., 2018).
573
574 **Cell culture, transfection and drug treatment**
575 Primary hippocampal neurons were cultured as previously described (Yang et al., 2021).
576 Briefly, Hippocampi of female or male pups (P0) were rapidly dissected under sterile
577 conditions, kept in cold DMEM (4°C) with high glucose. Tissue was then digested with
578 0.25% trypsin solution at 37°C for 18-20 min, triturated in DMEM supplemented with
579 10% F12 (11765054, Gibco) and 10% FBS (Gibco, Carlsbad, CA, USA). Then the
580 tissue was mechanically dissociated into single cells by gentle pipetting up and down.
581 Neurons were plated at a density of ~3.0-3.5× 10^5 cells/well in poly-D-lysine (P6407,

582 Sigma-Aldrich) -coated 6-well plate and at a density of 2.5–3.0×10^4 cells/well in 24-
583 well plate. Four hours later, media was changed to Neurobasal A (NB-A) growth
584 medium supplemented with 2% B27 supplement (17504-044, Gibco), 1% GlutaMAX
585 (35050-061, Gibco) and 33 mM glucose. Culture media were changed by half volume
586 with Neurobasal maintenance media once a week. The cultures were maintained at
587 37°C with 5% CO_2. Experiments were performed at DIV 14-16 unless otherwise stated.
588 For neuronal transfection, hippocampal neurons (DIV11) were transfected using
589 Lipofectamine-LTX (15338100, Invitrogen, ThermoFisher Scientific). For 12 mm
590 coverslips in individual wells of a 24 well plate, 0.5 μg of DNA was mixed with 0.5 μL
591 PLUS reagent in 50 μL of NB-A and incubated for 5 min at RT, then gently mixed with
592 1 μL Lipofectamine LTX in 50 μL NB-A and incubated for 20 min at RT. The DNA-
593 Lipofectamine LTX mixture was then added to the neurons in NB-A at 37°C in 5% CO_2
594 for 1 h. Neurons were then rinsed with NB-A and incubated in the original medium at
595 37°C in 5% CO_2 for 3-4 days.
596 For HEK293T cell culture, DMEM supplemented with 10% FBS were used. Cell
597 transfections were performed using Lipofectamine-2000 (11668019, Invitrogen,
598 ThermoFisher Scientific) according to the manufacturer's instructions. Cells were
599 harvested 24-48 h post transfection.
600 For inhibitor treatment, primary neurons cultured on coverslips were pre-incubated
601 with Latrunculin A (1 μM, 76343-93-6, Sigma-Aldrich), Nocodazole (1 μM, 31430-18-
602 9, Sigma-Aldrich) for 60 min or 120 min.
603
604 **Immunofluorescence staining of cultured neurons**
605 Hippocampal neurons were fixed in 4% paraformaldehyde/4% sucrose in PBS at RT
606 for 15 min, then permeabilized in 0.4% Triton X-100 in PBS for 10 min. After blocking
607 with 2% BSA in PBS containing 0.4% Triton X-100 for 30 min at RT, neurons were
608 incubated with primary antibodies for 1 h at RT or overnight at 4°C, and appropriate
609 secondary antibodies conjugated with Alexa Fluor 488, Alexa Fluor 555, or Alexa Fluor
610 647 were used for detection. The primary antibody was diluted in a PBS-2% BSA

611 solution and incubated overnight at 4°C. After washing with PBS three times, samples
612 were incubated with Alexa Fluor secondary antibodies (1:2000, Thermo Fisher) for 1 h
613 at RT, and mounted without bubbles.
614
615 **Biotinylation of cell surface proteins**
616 Surface biotinylation experiments were performed as previously described (Guo et al.,
617 2022). Briefly, Neurons were washed with ice cold extracellular solution (ECS) (in mM:
618 125 NaCl, 2 $CaCl_2$, 2.5 KCl, 5 HEPES, 33 glucose, pH, 8.0) and incubated for 30 min
619 with 0.8 mg/ml NHS-SS-Biotin (21327, Thermo Fisher Scientific) in ECS buffer at
620 37°C. After incubation, cells were washed once with PBS and the unbound biotin was
621 quenched via two 8 min incubations with quenching buffer (20 mM glycine in PBS).
622 Lysis was performed by mechanical scraping in ice-cold lysis buffer (50 mM Tris-Cl
623 pH 7.4, 150 mM NaCl, 1% TritonX-100, 0.1% SDS). After rotating for 30 min at 4°C,
624 lysates were centrifuged for 10 min at 14,000× *g* at 4°C. Balanced Pierce Streptavidin
625 Agarose beads (25 μL, 20353, Thermo Fisher Scientific) were added to the supernatant.
626 The mixture of lysates and beads were rotated at 4°C overnight and then washed twice
627 with ice-cold lysis buffer. Beads were incubated with 2× SDS sample buffer for 10 min
628 at 37°C and biotinylated proteins were analyzed by immunoblotting.
629
630 **Protein expression and purification**
631 GST-tagged EndoA1 or gephyrin fragments was expressed in *E. coli* BL21 (DE3). Cells
632 were grown at 37°C in LB (g/L: tryptone 10, yeast extract 5, NaCl 10) supplemented
633 with ampicillin. Cells were induced at OD600 of ~0.6 with 0.4 mM isopropyl-D-1-
634 thiogalactopyranoside (IPTG, A600168-0005, Bio Basic Inc) for 4 h at 30°C or 16 h at
635 16°C. Cell pellets were resuspended in PBS supplemented with 0.2% Triton X-100 and
636 0.1 mM PMSF. Proteins were purified with Glutathione Sepharose 4B (GE17-0756-01,
637 Sigma-Aldrich, St. Louis, MO, USA) according to the manufacturer's instructions.
638
639 **GST-pull down, co-immunoprecipitation (IP) and immunoisolation**

640 For GST-pull down assays, GST-fused protein EndoA1 and its fragments were
641 expressed and purified from *E. coli*. Myc-tagged GPN constructs were expressed in
642 HEK293 cells for 48 h and lysates were prepared in a buffer (in mM: Tris-HCl 50, pH
643 7.4, NaCl 150, 1% NP-40, EDTA 2) plus protease inhibitors cocktail. Cell lysates were
644 centrifuged at 12,000× *g* for 15 min at 4°C and the supernatant was incubated with
645 individual GST-fused proteins conjugated with Glutathione-Sepharose beads for
646 overnight at 4°C. Beads were washed five times with lysis buffer and boiled in 2× SDS
647 sample buffer. Bound proteins were analyzed by immunoblotting.

648 For co-IP from brain lysates, the whole brain from 8-10-week-old WT and KO
649 littermates were dissected and homogenized in the pre-chilled lysis buffer (in mM: Tris-
650 HCl 20, pH 7.4, NaCl 150, 1% NP-40, EDTA 5) plus protease inhibitor cocktail,
651 followed by incubation on ice for 15 min. The lysates were then centrifuged at 12,000×
652 *g* for 15 min and the supernatant was collected and incubated with anti-EndoA1
653 antibody (2 μg) or control IgG overnight at 4°C, followed by incubation with 20 μL
654 Dynabeads Protein A (ThermoFisher, 10007D for rabbit antibody) for 2 h at 4°C. After
655 washing the beads with the same lysis buffer four times, the bound proteins were
656 incubated 2× SDS sample buffer at 37°C for 10 min and subjected to SDS-PAGE and
657 Western blot with indicated antibodies.

658 For co-IP of proteins in HEK293T cells (Cat. No. 632180, Takara), cells were lysed
659 with lysis buffer (in mM: 0.5% NP-40, Tris-HCl 50, pH 7.4, NaCl 150, EDTA 5)
660 supplemented with protease inhibitors. Lysates were then centrifuged at 16,000× *g* for
661 15 min at 4°C. Cell lysates were incubated with anti-Flag Affinity Gel (A2220, Sigma-
662 Aldrich) overnight at 4°C on a roller mixer. Immunoprecipitates were washed four
663 times in lysis buffer and boiled in 2× SDS sample buffer, then subjected to SDS-PAGE
664 and immunoblotting.

665 For immunoisolation of membrane proteins, hippocampi were homogenized with
666 lysis buffer (in mM: Tris-HCl 20, pH 7.4, HEPES 10, pH 7.4, NaCl 150, sucrose 250,
667 EDTA 0.5, pH 8.0) supplemented with protease inhibitors and centrifuged at 800× *g* for
668 15 min. The supernatants were collected and subjected to high-speed centrifugation at

669 100,000× *g* for 1 h (TLS-55 rotor, OptimaTMMAX Ultracentrifuge; Beckman Coulter,
670 USA). The supernatants (S100) and pellets (P100, the membrane fraction) resuspended
671 in lysis buffer were subjected to immunoisolation with Dynabeads Protein A (100-4D,
672 Invitrogen, Carlsbad, CA, USA) coupled with 2 μg of rabbit anti-EndoA1 or rabbit anti-
673 $GABA_AR$ α1 antibody. Bound proteins were eluted by incubation with 2× SDS loading
674 buffer at 37°C for 10 min and subjected to SDS-PAGE and immunoblotting.
675
676 **PSD fractionation of brain lysates**
677 PSD fractions from adult mouse brain were prepared as previously described (Yang et
678 al., 2015). In brief, hippocampi were homogenized on ice with 20 strokes of a Teflon-
679 glass homogenizer in 1 mL of HEPES-buffered sucrose (0.32 M sucrose, 4 mM HEPES,
680 pH 7.4) containing freshly added protease inhibitors, then centrifuged at 800× *g* at 4°C
681 to remove the pelleted nuclear fraction (P1). Supernatant (S1) was centrifuged at
682 10,000× *g* for 15 min to yield the crude synaptosomal pellet (P2) and the pellet was
683 washed once in 1 mL HEPES-buffered sucrose. P2 was lysed by hypoosmotic shock in
684 900 μL ice-cold 4 mM HEPES, pH 7.4 plus protease inhibitors, homogenized by
685 pipetting and rotating for 30 min at 4 °C. The lysate was centrifuged at 25,000× *g* for
686 20 min to yield supernatant (S3, crude synaptic vesicle fraction) and pellet (P3, lysed
687 synaptosomal membrane fraction). To prepare the PSD fraction, P3 was resuspended in
688 900 μL of ice-cold 50 mM HEPES, pH 7.4, 2 mM EDTA, plus protease inhibitors and
689 0.5% Triton X-100, rotated for 15 min at 4 °C and centrifuged at 32,000× *g* for 20 min
690 to obtain the PSD pellet. PSD pellets were resuspended in 50 μL ice-cold 50 mM
691 HEPES, pH 7.4, 2 mM EDTA plus protease inhibitors. Proteins were subjected to SDS-
692 PAGE and immunoblotting.
693
694 **Protein identification with mass spectrometry and pathway analysis**
695 For identification of EndoA1-interacting proteins, mouse brain was homogenized with
696 lysis buffer (in mM: Tris-HCl 20, pH 7.4, HEPES 10, pH 7.4, NaCl 150, EDTA 1, 1%
697 NP-40) supplemented with protease inhibitors. Lysates were centrifuged at 12,000× *g*

698 for 15 min. The supernatants were incubated with rabbit anti-EndoA1 antibody
699 overnight at 4°C. Beads were rinsed with lysis buffer for five times and bound proteins
700 were resolved by SDS-PAGE. Proteins in the gels were reduced with 10 mM DTT at
701 37°C for 1 h, then alkylated with 25 mM iodoacetamide at RT for 1 h in the dark before
702 digestion with trypsin (T1426, Sigma-Aldrich; enzyme-to-substrate ratio 1:50) in 25
703 mM ammonium bicarbonate at 37°C overnight. Tryptic peptides were extracted from
704 gel by sonication with a buffer containing 5% trifluoroacetic acid and 50% acetonitrile.
705 The liquid was dried by SpeedVac, and peptides were resolubilized in 0.1% formic acid
706 and filtered with 0.45 μm centrifugal filters before analysis with a TripleTOF 5600 mass
707 spectrometer (AB SCIEX, Canada) coupled to an Eksigent nanoLC. Proteins were
708 identified by searching the MS/MS spectra against the *Mus musculus* SwissProt
709 database using the ProteinPilot 4.2 software. Carbamidomethylation of cysteine was set
710 as the fixed modification. Trypsin was specified as the proteolytic enzyme with a
711 maximum of 2 miss cleavages. Mass tolerance was set to 0.05 Da and the false
712 discovery rates for both proteins and peptides were set at 1%. For enrichment pathway
713 analysis: Only proteins with intensity to IgG ratio of > 1.5 were considered in the
714 analysis. These genes were analyzed by Gene Ontology (GO) Enrichment Analysis
715 (http://bioinfo.org/kobas).
716

717 **Electrophysiology**

718 To knockout *EndoA1* in the brain, *EndoA1*$^{fl/fl}$ mice were injected with high-titer AAV
719 stock carrying pAOV-CaMKIIα-mCherry-2A-Cre (AAV-mCherry-2A-Cre) (1~5 × 10^{13}
720 IU/ml) in the hippocampal CA1 region within 24 h after birth. Newborn *EndoA1*$^{fl/fl}$
721 littermates (male or female) were anesthetized on ice for 4-5 min and then mounted in
722 a custom ceramic mold to align the head along the X and Y axes, with lambda set as (X,
723 Y) = (0, 0). The zero point of the Z axis was the position at which the injecting needle
724 penetrated the skin. Approximately 10 nL of the viral solution was injected at each of
725 the seven sites (coordinates in mm, [X, Y, Z] = [1.2, 1.2, 1.4/1.0/0.6] and [1.5, 1.0,
726 1.7/1.3/0.9/0.5]) targeting the hippocampus in each cerebral hemisphere using a

727 microsyringe (Sutter Instrument, Novato, CA, USA) and beveled glass injection pipette
728 (Yang et al., 2018). For the rescue experiment, P0 *EndoA1*$^{fl/fl}$ mice were injected with a
729 mixture of two high-titer AAV stocks: AAV-EGFP and AAV-mCherry or AAV-
730 mCherry-2A-Cre; AAV-mCherry-2A-Cre and AAV-EGFP-2A-FLAG-EndoA1, AAV-
731 EGFP-2A-FLAG-EndoA1 Y343A or AAV-EGFP-2A-FLAG-EndoA1 KKK-EEE.
732 Approximately 20 nL of the viral solution was injected at each of the seven sites. The
733 injected pups were returned to the home cage and used for recording 2 weeks later.

734 To prepare acute brain slices for electrophysiological analyses, mice were
735 anesthetized with tribromoethanol (330-390 mg/kg) (T48402, Sigma-Aldrich, St. Louis,
736 MO, USA) and decapitated. Whole brains were removed promptly and placed in ice-
737 cold oxygenated (95% O_2/5% CO_2) low-Ca^{2+}/high-Mg^{2+} high-sucrose cutting solution
738 (in mM: KCl 2.5, $NaHCO_3$ 25, NaH_2PO_4 1.25, glucose 10, sucrose 210, Na-Ascorbate
739 1.3, $CaCl_2$ 0.5, $MgSO_4$ 7). Coronal 300 μm slices were obtained using a vibrating tissue
740 slicer (Leica VT1200S; Leica Biosystems, Wetzlar, Deutschland). Slices were
741 immediately transferred to standard artificial cerebrospinal fluid (ACSF) (in mM: NaCl
742 119, KCl 2.5, $MgSO_4$ 1.3, $CaCl_2$ 2.5, glucose 11, $NaHCO_3$ 26.2, NaH_2PO_4 1, pH 7.3-
743 7.4) at 33°C and continuously bubbled with 95% O_2/5% CO_2. After 30 min of
744 incubation, slices were transferred to a recording chamber with the same extracellular
745 buffer at room temperature (RT, ~25°C).

746 For whole-cell patch clamp recordings, brain slices were continuously perfused
747 with standard ACSF at RT under visual control with differential interference contrast
748 illumination on an upright microscope (BX51WI, Olympus, Tokyo, Japan) with a 40×
749 water-immersion objective and a digital camera. The mCherry- and/or EGFP-positive
750 hippocampal CA1 pyramidal neurons were identified by an epifluorescence microscope
751 (pE-300, CoolLED Ltd, Andover, UK). Whole-cell recordings were performed on an
752 AAV-infected neuron and a neighboring uninfected neuron. Patch clamp data were
753 obtained using a Multiclamp 700B amplifier (Molecular Devices, San Jose, CA, USA),
754 and signals were low-pass filtered at 2 kHz and digitized at 10 kHz using an Axon
755 Digidata 1550B analog-to-digital board (Molecular Devices, San Jose, CA, USA).

To analyze evoked excitatory postsynaptic currents (eEPSCs), evoked inhibitory postsynaptic currents (eIPSCs), and paired-pause ratio, cells were recorded with 3-7 MΩ borosilicate glass patch pipettes filled with the intracellular solution (in mM: $CsMeSO_3$ 135, HEPES 10, EGTA 1, QX-314 3.3, MgATP 4, NaGTP 0.3, and Na_2-phosphocreatine 8, pH 7.3) (Horn and Nicoll, 2018), following stimulation of Schaffer collaterals with a bipolar stimulation electrode placed in the stratum radiatum of the CA1 region. EPSCs were measured at a holding potential of -70 mV, and IPSCs were recorded at +10 mV. Paired-pulse ratios of EPSCs were measured at a holding potential of -70 mV by applying two electrical stimulations at a 50 ms interval and calculating the ratio of the peak amplitudes. Paired-pulse ratios of IPSCs were measured at a holding potential of +10 mV by applying two electrical stimulations at a 200 ms interval and calculating the ratio of the peak amplitudes. E/I ratios were measured by applying the same stimulation current and then calculating the ratio of the absolute values of the peak amplitudes of EPSCs and IPSCs. The miniature EPSCs and IPSCs were measured in the ACSF bath solution containing 1 μM tetrodotoxin (TTX, MSS0002, BGB Analytik AG, BL, Switzerland) at -70 mV and +10 mV, respectively, in the voltage-clamp mode. Data were collected and analyzed using the pClamp 10.6 software (Molecular Devices, San Jose, CA, USA).

All electrophysiological recordings were carried out blindly and all n numbers in the data figures indicate the number of recorded neurons. All chemicals were purchased from Sigma-Aldrich except otherwise noted.

Confocal and three-dimensional structured illumination microscopy (3D-SIM) image acquisition and analysis

Confocal images were collected using the Spectral Imaging Confocal Microscope Digital Eclipse A1Si (Nikon, Tokyo, Japan) with a 100× Plan Apochromat VC (NA 1.40) oil objective (4× optical zoom). Images were z projections of images taken at 0.25-μm step intervals. The number of planes, typically 5-7, was chosen to cover the entire dendrite from top to bottom. Images were captured using a 1024×1024 pixels screen

785 for neuronal cells. Laser power, digital gain, and offset settings were identical in each
786 experiment. Images were processed with the NIH ImageJ software and exported into
787 Adobe Photoshop. Only brightness and contrast were adjusted for the whole frame, and
788 no part of a frame was enhanced or modified in any way. Control and experimental
789 group neurons which were to be directly compared were imaged with the same
790 acquisition parameters.

791 For 3D-SIM, secondary antibodies conjugated with Alexa Fluor 568 were used
792 and images were captured as described by Niu et al (Niu et al., 2017) on the DeltaVision
793 OMX V4 imaging system (Applied Precision Inc, USA) with a 100× 1.4 oil objective
794 (Olympus UPlanSApo), solid state multimode lasers (488, 593 and 642 nm) and
795 electron-multiplying charge-coupled device (CCD) cameras (Evolve 512× 512,
796 Photometrics, USA). Serial Z-stack sectioning was done at 125 nm intervals. The
797 microscope is routinely calibrated with 100 nm fluorescent spheres to calculate both
798 the lateral and axial limits of image resolution. SIM image stacks were reconstructed
799 using softWoRx 5.0 (Applied Precision) with the following settings: pixel size 39.5 nm;
800 channel-specific optical transfer functions; Wiener filter 0.001000; discard Negative
801 Intensities background; drift correction with respect to first angle; custom K0 guess
802 angles for camera positions. Pixel registration was corrected to be less than 1 pixel for
803 all channels using 100 nm Tetraspeck beads. Three dimensional images were
804 reconstructed from z stacks. For clarity of display, small linear changes of brightness
805 and contrast were performed on three-dimensional reconstructions.

806 Quantification of immunostaining were carried out blindly. For quantitative
807 analysis of immunofluorescent signals in neurons, maximal projection images were
808 created with the ImageJ software (https://imagej.net.) from 6-7 serial optical sections.
809 Background was subtracted by using the "subtract background" function and the
810 background level was held identical for all cells within each experiment. To examine
811 the number and fluorescence intensity of signal puncta in soma or dendrites, the EGFP-
812 or DsRed-labeled soma or dendrites were outlined automatically by using the "Wand
813 Tool" function. The region of interest (ROI) in cultured neurons was defined along a

segment of the dendrite according to the fluorescence signal distinguished from the background. Average values of fluorescence intensities in ROI (the total fluorescent intensity divided by the total area of a dendritic segment) were calculated by Analyze > measure. Gephyrin clusters were thresholded and confirmed visually to select appropriate clusters following a minimal size cut-off by using the "Analyze Particles" plugin of the ImageJ software. For colocalization quantifications, NIS-Elements Software was used as follows: region of interest (ROI) of dendritic segments was manually chosen, and thresholded using the "Threshold" function to remove background signals. Pearson's correlation coefficient and Manders overlap coefficient were analyzed by using the "Analyze Control > colocalization" function.

For spatial correlation/colocalization analysis in super-resolution images, we using the method described in the reference (McCall, 2024). Briefly, channels in 3D images were split and followed by Gaussian blur performed on both GPN and Bassoon channels. Next masks of all possible localizations for the signal in GPN and Bassoon image channel were obtained. Then, the input images of the three channels were deconvolved using 10 iterations of the Richardson-Lucy algorithm in Deconvolution Lab 2 (version 2.1.2), with theoretical point spread functions (PSFs) generated by the PSF Generator plugin. PSFs were generated using the Born & Wolf model, with parameters matching the acquisition parameters: 1.518 immersion refractive index, 1.4 NA, 40 nm pixel size and 125 nm z-step, 512 × 512 × 14 output diameters, and 520 nm, 592 nm and 670 nm wavelengths. Finaly, select the two images (GPN and EndoA1 or Bassoon and EndoA1) and the mask images, then perform a cross-correlation analysis (CCC) between the two images using the CCC plugin (https://github.com/andmccall/Colocalization_by_Cross_Correlation).

Statistical analysis

For all biochemical, cell biological and electrophysiological recordings, at least three independent experiments were performed (independent cultures, transfections or different mice). Statistical analysis was performed in GraphPad Prism 9.0 (GraphPad

Software, La Jolla, CA). Data sets were tested for normality and direct comparisons between two groups were made using two-tailed Student's t test (t test, for normally distributed data) as indicated. To evaluate statistical significance of three or more groups of samples, one-way ANOVA analysis with a Tukey test was used or repeated measures ANOVA analysis with a Tukey test was used in behavior assays. Statistical parameters are reported in the figures and the corresponding legends. The statistical significance was defined as * $p < 0.05$, ** $p < 0.01$, *** $p < 0.001$, respectively. All data are presented as scatterplots with mean ± S.E.M.

Acknowledgments

We thank Drs Shiva Tyagarajan (Addgene #68816), Peter Scheiffele (Addgene # 15246) and Don Arnold (Addgene # 46295 & #46296) for constructs. This work was supported by funding from the National Natural Science Foundation of China (NSFC 32271005 and 32070785 to Y. Yang, 31921002, 32270730 and 91954126 to J-J. Liu) and the State Key Laboratory of Molecular Developmental Biology (2022-MDB-KF-13).

The authors declare no competing financial interests.

Author contributions: J-J. Liu and Y. Yang conceived the project. Y. Yang and J-J. Liu designed and supervised research. X. Chen, D. Pan and Y. Yang performed experiments and analyzed the data. Y. Yang and J-J. Liu wrote the manuscript with help from all other authors.

References

Allison, D.W., Chervin, A.S., Gelfand, V.I., and Craig, A.M. (2000). Postsynaptic scaffolds of excitatory and inhibitory synapses in hippocampal neurons: maintenance of core components independent of actin filaments and microtubules. The Journal of neuroscience : the official journal of the Society for Neuroscience *20*, 4545-4554.

Bademosi, A.T., Decet, M., Kuenen, S., Calatayud, C., Swerts, J., Gallego, S.F., Schoovaerts, N., Karamanou, S., Louros, N., Martin, E., *et al.* (2023). EndophilinA-dependent coupling between activity-induced calcium influx and synaptic autophagy is disrupted by a Parkinson-risk mutation. Neuron.

Bai, G., Wang, Y., and Zhang, M. (2021). Gephyrin-mediated formation of inhibitory postsynaptic density sheet via phase separation. Cell research *31*, 312-325.

Bensussen, S., Shankar, S., Ching, K.H., Zemel, D., Ta, T.L., Mount, R.A., Shroff, S.N., Gritton, H.J., Fabris, P., Vanbenschoten, H.*, et al.* (2020). A Viral Toolbox of Genetically Encoded Fluorescent Synaptic Tags. iScience *23*, 101330.

Bogdanov, Y., Michels, G., Armstrong-Gold, C., Haydon, P.G., Lindstrom, J., Pangalos, M., and Moss, S.J. (2006). Synaptic GABAA receptors are directly recruited from their extrasynaptic counterparts. The EMBO journal *25*, 4381-4389.

Canitano, R., and Pallagrosi, M. (2017). Autism Spectrum Disorders and Schizophrenia Spectrum Disorders: Excitation/Inhibition Imbalance and Developmental Trajectories. Frontiers in psychiatry *8*, 69.

Canitano, R., and Palumbi, R. (2021). Excitation/Inhibition Modulators in Autism Spectrum Disorder: Current Clinical Research. Frontiers in neuroscience *15*, 753274.

Chang, D., Nalls, M.A., Hallgrímsdóttir, I.B., Hunkapiller, J., van der Brug, M., Cai, F., Kerchner, G.A., Ayalon, G., Bingol, B., Sheng, M.*, et al.* (2017). A meta-analysis of genome-wide association studies identifies 17 new Parkinson's disease risk loci. Nature genetics *49*, 1511-1516.

Charrier, C., Ehrensperger, M.V., Dahan, M., Lévi, S., and Triller, A. (2006). Cytoskeleton regulation of glycine receptor number at synapses and diffusion in the plasma membrane. J Neurosci *26*, 8502-8511.

Chen, J.L., Villa, K.L., Cha, J.W., So, P.T., Kubota, Y., and Nedivi, E. (2012). Clustered dynamics of inhibitory synapses and dendritic spines in the adult neocortex. Neuron *74*, 361-373.

Chih, B., Gollan, L., and Scheiffele, P. (2006). Alternative splicing controls selective trans-synaptic interactions of the neuroligin-neurexin complex. Neuron *51*, 171-178.

Corponi, F., Bonassi, S., Vieta, E., Albani, D., Frustaci, A., Ducci, G., Landi, S., Boccia, S., Serretti, A., and Fabbri, C. (2019). Genetic basis of psychopathological dimensions shared between schizophrenia and bipolar disorder. Prog Neuropsychopharmacol Biol Psychiatry *89*, 23-29.

Cramer, T.M.L., Pinan-Lucarre, B., Cavaccini, A., Damilou, A., Tsai, Y.C., Bhat, M.A., Panzanelli, P., Rama, N., Mehlen, P., Benke, D.*, et al.* (2023). Adamtsl3 mediates DCC signaling to selectively promote GABAergic synapse function. Cell reports *42*, 112947.

Dhir, A. (2012). Pentylenetetrazol (PTZ) kindling model of epilepsy. Curr Protoc Neurosci *Chapter 9*, Unit9.37.

Essrich, C., Lorez, M., Benson, J.A., Fritschy, J.M., and Luscher, B. (1998). Postsynaptic clustering of major GABAA receptor subtypes requires the gamma 2 subunit and gephyrin. Nature neuroscience *1*, 563-571.

Favuzzi, E., Deogracias, R., Marques-Smith, A., Maeso, P., Jezequel, J., Exposito-Alonso, D., Balia, M., Kroon, T., Hinojosa, A.J., E, F.M.*, et al.* (2019). Distinct molecular programs regulate synapse specificity in cortical inhibitory circuits. Science *363*, 413-417.

Foss-Feig, J.H., Adkinson, B.D., Ji, J.L., Yang, G., Srihari, V.H., McPartland, J.C., Krystal, J.H., Murray, J.D., and Anticevic, A. (2017). Searching for Cross-Diagnostic Convergence: Neural Mechanisms Governing Excitation and Inhibition Balance in Schizophrenia and Autism Spectrum Disorders. Biol Psychiatry *81*, 848-861.

Fritschy, J.M. (2008). Epilepsy, E/I Balance and GABA(A) Receptor Plasticity. Frontiers in molecular neuroscience *1*, 5.

Gad, H., Ringstad, N., Low, P., Kjaerulff, O., Gustafsson, J., Wenk, M., Di Paolo, G., Nemoto, Y., Crun,

919 J., Ellisman, M.H., *et al.* (2000). Fission and uncoating of synaptic clathrin-coated vesicles are
920 perturbed by disruption of interactions with the SH3 domain of endophilin. Neuron *27*, 301-312.
921 George, S., Chiou, T.T., Kanamalla, K., and De Blas, A.L. (2021). Recruitment of Plasma Membrane
922 GABA-A Receptors by Submembranous Gephyrin/Collybistin Clusters. Cellular and molecular
923 neurobiology.
924 Germer, E.L., Imhoff, S., Vilariño-Güell, C., Kasten, M., Seibler, P., Brüggemann, N., Klein, C., and
925 Trinh, J. (2019). The Role of Rare Coding Variants in Parkinson's Disease GWAS Loci. Frontiers in
926 neurology *10*, 1284.
927 Gross, G.G., Junge, J.A., Mora, R.J., Kwon, H.B., Olson, C.A., Takahashi, T.T., Liman, E.R., Ellis-Davies,
928 G.C., McGee, A.W., Sabatini, B.L., *et al.* (2013). Recombinant probes for visualizing endogenous
929 synaptic proteins in living neurons. Neuron *78*, 971-985.
930 Gu, J., Firestein, B.L., and Zheng, J.Q. (2008). Microtubules in dendritic spine development. J
931 Neurosci *28*, 12120-12124.
932 Guo, Z., Jiang, C.H., Tong, C., Yang, Y., Wang, Z., Lam, S.M., Wang, D., Li, R., Shui, G., Shi, Y.S., *et al.*
933 (2022). Activity-dependent PI4P synthesis by PI4KIIIα regulates long-term synaptic potentiation.
934 Cell Rep *38*, 110452.
935 Han, W., Li, J., Pelkey, K.A., Pandey, S., Chen, X., Wang, Y.X., Wu, K., Ge, L., Li, T., Castellano, D., *et*
936 *al.* (2019). Shisa7 is a GABA(A) receptor auxiliary subunit controlling benzodiazepine actions.
937 Science *366*, 246-250.
938 Hoffmann, C., and Milovanovic, D. (2021). Gephyrin: a scaffold that builds a phase at the inhibitory
939 postsynapses. Cell research *31*, 245-246.
940 Horn, M.E., and Nicoll, R.A. (2018). Somatostatin and parvalbumin inhibitory synapses onto
941 hippocampal pyramidal neurons are regulated by distinct mechanisms. Proceedings of the
942 National Academy of Sciences *115*, 589-594.
943 Huo, J.Z., Cortez, M.A., and Snead, O.C., 3rd (2009). GABA receptor proteins within lipid rafts in the
944 AY-9944 model of atypical absence seizures. Epilepsia *50*, 776-788.
945 Jacob, T.C., Bogdanov, Y.D., Magnus, C., Saliba, R.S., Kittler, J.T., Haydon, P.G., and Moss, S.J. (2005).
946 Gephyrin regulates the cell surface dynamics of synaptic GABAA receptors. J Neurosci *25*, 10469-
947 10478.
948 Jaworski, J., Kapitein, L.C., Gouveia, S.M., Dortland, B.R., Wulf, P.S., Grigoriev, I., Camera, P., Spangler,
949 S.A., Di Stefano, P., Demmers, J., *et al.* (2009). Dynamic microtubules regulate dendritic spine
950 morphology and synaptic plasticity. Neuron *61*, 85-100.
951 Kalscheuer, V.M., Musante, L., Fang, C., Hoffmann, K., Fuchs, C., Carta, E., Deas, E., Venkateswarlu,
952 K., Menzel, C., Ullmann, R., *et al.* (2009). A balanced chromosomal translocation disrupting
953 ARHGEF9 is associated with epilepsy, anxiety, aggression, and mental retardation. Human
954 mutation *30*, 61-68.
955 Kasaragod, V.B., Mortensen, M., Hardwick, S.W., Wahid, A.A., Dorovykh, V., Chirgadze, D.Y., Smart,
956 T.G., and Miller, P.S. (2022). Mechanisms of inhibition and activation of extrasynaptic alphabeta
957 GABA(A) receptors. Nature *602*, 529-533.
958 Kasaragod, V.B., and Schindelin, H. (2019). Structure of Heteropentameric GABAA Receptors and
959 Receptor-Anchoring Properties of Gephyrin. Frontiers in molecular neuroscience *12*, 191.
960 Kins, S., Betz, H., and Kirsch, J. (2000). Collybistin, a newly identified brain-specific GEF, induces
961 submembrane clustering of gephyrin. Nat Neurosci *3*, 22-29.
962 Kirsch, J., and Betz, H. (1995). The postsynaptic localization of the glycine receptor-associated

963 protein gephyrin is regulated by the cytoskeleton. The Journal of neuroscience : the official journal
964 of the Society for Neuroscience *15*, 4148-4156.
965 Kirsch, J., Langosch, D., Prior, P., Littauer, U.Z., Schmitt, B., and Betz, H. (1991). The 93-kDa glycine
966 receptor-associated protein binds to tubulin. The Journal of biological chemistry *266*, 22242-
967 22245.
968 Klausberger, T., and Somogyi, P. (2008). Neuronal diversity and temporal dynamics: the unity of
969 hippocampal circuit operations. Science *321*, 53-57.
970 Kneussel, M., Brandstätter, J.H., Laube, B., Stahl, S., Müller, U., and Betz, H. (1999). Loss of
971 Postsynaptic GABAAReceptor Clustering in Gephyrin-Deficient Mice. J Neurosci *19*, 9289-9297.
972 Koh, W., Kwak, H., Cheong, E., and Lee, C.J. (2023). GABA tone regulation and its cognitive functions
973 in the brain. Nature reviews Neuroscience *24*, 523-539.
974 Liu, Y.T., Tao, C.L., Zhang, X., Xia, W., Shi, D.Q., Qi, L., Xu, C., Sun, R., Li, X.W., Lau, P.M.*, et al.* (2020).
975 Mesophasic organization of GABAA receptors in hippocampal inhibitory synapses. Nat Neurosci
976 *23*, 1589-1596.
977 Loebrich, S., Bahring, R., Katsuno, T., Tsukita, S., and Kneussel, M. (2006). Activated radixin is
978 essential for GABAA receptor alpha5 subunit anchoring at the actin cytoskeleton. The EMBO
979 journal *25*, 987-999.
980 McCall, A.D. (2024). Colocalization by cross-correlation, a new method of colocalization suited for
981 super-resolution microscopy. BMC bioinformatics *25*, 55.
982 Miles, R., Tóth, K., Gulyás, A.I., Hájos, N., and Freund, T.F. (1996). Differences between somatic and
983 dendritic inhibition in the hippocampus. Neuron *16*, 815-823.
984 Milosevic, I., Giovedi, S., Lou, X., Raimondi, A., Collesi, C., Shen, H., Paradise, S., O'Toole, E.,
985 Ferguson, S., Cremona, O.*, et al.* (2011). Recruitment of endophilin to clathrin-coated pit necks is
986 required for efficient vesicle uncoating after fission. Neuron *72*, 587-601.
987 Mody, I., and Pearce, R.A. (2004). Diversity of inhibitory neurotransmission through GABA(A)
988 receptors. Trends in neurosciences *27*, 569-575.
989 Mukherjee, J., Kretschmannova, K., Gouzer, G., Maric, H.M., Ramsden, S., Tretter, V., Harvey, K.,
990 Davies, P.A., Triller, A., Schindelin, H.*, et al.* (2011). The residence time of GABA(A)Rs at inhibitory
991 synapses is determined by direct binding of the receptor α1 subunit to gephyrin. J Neurosci *31*,
992 14677-14687.
993 Murdoch, J.D., Rostosky, C.M., Gowrisankaran, S., Arora, A.S., Soukup, S.F., Vidal, R., Capece, V.,
994 Freytag, S., Fischer, A., Verstreken, P.*, et al.* (2016). Endophilin-A Deficiency Induces the Foxo3a-
995 Fbxo32 Network in the Brain and Causes Dysregulation of Autophagy and the Ubiquitin-
996 Proteasome System. Cell reports *17*, 1071-1086.
997 Niu, Y., Dai, Z., Liu, W., Zhang, C., Yang, Y., Guo, Z., Li, X., Xu, C., Huang, X., Wang, Y.*, et al.* (2017).
998 Ablation of SNX6 leads to defects in synaptic function of CA1 pyramidal neurons and spatial
999 memory. eLife *6*.
1000 Nusser, Z., Hajos, N., Somogyi, P., and Mody, I. (1998). Increased number of synaptic GABA(A)
1001 receptors underlies potentiation at hippocampal inhibitory synapses. Nature *395*, 172-177.
1002 Parato, J., and Bartolini, F. (2021). The microtubule cytoskeleton at the synapse. Neuroscience
1003 letters *753*, 135850.
1004 Poulopoulos, A., Aramuni, G., Meyer, G., Soykan, T., Hoon, M., Papadopoulos, T., Zhang, M.,
1005 Paarmann, I., Fuchs, C., Harvey, K.*, et al.* (2009). Neuroligin 2 drives postsynaptic assembly at
1006 perisomatic inhibitory synapses through gephyrin and collybistin. Neuron *63*, 628-642.

1007 Ren, Y., Xu, H.W., Davey, F., Taylor, M., Aiton, J., Coote, P., Fang, F., Yao, J., Chen, D., Chen, J.X., *et*
1008 *al.* (2008). Endophilin I expression is increased in the brains of Alzheimer disease patients. The
1009 Journal of biological chemistry *283*, 5685-5691.
1010 Ringstad, N., Gad, H., Low, P., Di Paolo, G., Brodin, L., Shupliakov, O., and De Camilli, P. (1999).
1011 Endophilin/SH3p4 is required for the transition from early to late stages in clathrin-mediated
1012 synaptic vesicle endocytosis. Neuron *24*, 143-154.
1013 Ringstad, N., Nemoto, Y., and De Camilli, P. (1997). The SH3p4/Sh3p8/SH3p13 protein family:
1014 binding partners for synaptojanin and dynamin via a Grb2-like Src homology 3 domain. Proc Natl
1015 Acad Sci U S A *94*, 8569-8574.
1016 Russo, I., Gavello, D., Menna, E., Vandael, D., Veglia, C., Morello, N., Corradini, I., Focchi, E., Alfieri,
1017 A., Angelini, C., *et al.* (2019). p140Cap Regulates GABAergic Synaptogenesis and Development of
1018 Hippocampal Inhibitory Circuits. Cerebral Cortex *29*, 91-105.
1019 Saiepour, L., Fuchs, C., Patrizi, A., Sassoè-Pognetto, M., Harvey, R.J., and Harvey, K. (2010). Complex
1020 role of collybistin and gephyrin in GABAA receptor clustering. J Biol Chem *285*, 29623-29631.
1021 Sakimoto, Y., Oo, P.M., Goshima, M., Kanehisa, I., Tsukada, Y., and Mitsushima, D. (2021).
1022 Significance of GABAA Receptor for Cognitive Function and Hippocampal Pathology. Int J Mol Sci
1023 *22*.
1024 Schulz, A., Miehl, C., Berry, M.J., 2nd, and Gjorgjieva, J. (2021). The generation of cortical novelty
1025 responses through inhibitory plasticity. eLife *10*.
1026 Schuske, K.R., Richmond, J.E., Matthies, D.S., Davis, W.S., Runz, S., Rube, D.A., van der Bliek, A.M.,
1027 and Jorgensen, E.M. (2003). Endophilin is required for synaptic vesicle endocytosis by localizing
1028 synaptojanin. Neuron *40*, 749-762.
1029 Scott, S., and Aricescu, A.R. (2019). A structural perspective on GABA(A) receptor pharmacology.
1030 Current opinion in structural biology *54*, 189-197.
1031 Sexton, C.A., Penzinger, R., Mortensen, M., Bright, D.P., and Smart, T.G. (2021). Structural
1032 determinants and regulation of spontaneous activity in GABAA receptors. Nature communications
1033 *12*, 5457.
1034 Soukup, S.F., Kuenen, S., Vanhauwaert, R., Manetsberger, J., Hernandez-Diaz, S., Swerts, J.,
1035 Schoovaerts, N., Vilain, S., Gounko, N.V., Vints, K., *et al.* (2016). A LRRK2-Dependent EndophilinA
1036 Phosphoswitch Is Critical for Macroautophagy at Presynaptic Terminals. Neuron *92*, 829-844.
1037 Spruston, N. (2008). Pyramidal neurons: dendritic structure and synaptic integration. Nature
1038 reviews Neuroscience *9*, 206-221.
1039 Tao, C.L., Liu, Y.T., Sun, R., Zhang, B., Qi, L., Shivakoti, S., Tian, C.L., Zhang, P., Lau, P.M., Zhou, Z.H.,
1040 *et al.* (2018). Differentiation and Characterization of Excitatory and Inhibitory Synapses by Cryo-
1041 electron Tomography and Correlative Microscopy. The Journal of neuroscience : the official journal
1042 of the Society for Neuroscience *38*, 1493-1510.
1043 Thomas, P., Mortensen, M., Hosie, A.M., and Smart, T.G. (2005). Dynamic mobility of functional
1044 GABAA receptors at inhibitory synapses. Nature neuroscience *8*, 889-897.
1045 Tretter, V., Jacob, T.C., Mukherjee, J., Fritschy, J.M., Pangalos, M.N., and Moss, S.J. (2008). The
1046 clustering of GABA(A) receptor subtypes at inhibitory synapses is facilitated via the direct binding
1047 of receptor alpha 2 subunits to gephyrin. The Journal of neuroscience : the official journal of the
1048 Society for Neuroscience *28*, 1356-1365.
1049 Tyagarajan, S.K., and Fritschy, J.M. (2014). Gephyrin: a master regulator of neuronal function? Nat
1050 Rev Neurosci *15*, 141-156.

1051 Tyagarajan, S.K., Ghosh, H., Yévenes, G.E., Imanishi, S.Y., Zeilhofer, H.U., Gerrits, B., and Fritschy,
1052 J.M. (2013). Extracellular signal-regulated kinase and glycogen synthase kinase 3β regulate
1053 gephyrin postsynaptic aggregation and GABAergic synaptic function in a calpain-dependent
1054 mechanism. The Journal of biological chemistry *288*, 9634-9647.
1055 van Bommel, B., Konietzny, A., Kobler, O., Bar, J., and Mikhaylova, M. (2019). F-actin patches
1056 associated with glutamatergic synapses control positioning of dendritic lysosomes. The EMBO
1057 journal *38*, e101183.
1058 Van Erum, J., Van Dam, D., and De Deyn, P.P. (2019). PTZ-induced seizures in mice require a revised
1059 Racine scale. Epilepsy & behavior : E&B *95*, 51-55.
1060 Verstreken, P., Koh, T.W., Schulze, K.L., Zhai, R.G., Hiesinger, P.R., Zhou, Y., Mehta, S.Q., Cao, Y.,
1061 Roos, J., and Bellen, H.J. (2003). Synaptojanin is recruited by endophilin to promote synaptic vesicle
1062 uncoating. Neuron *40*, 733-748.
1063 Wagner, S., Lee, C., Rojas, L., Specht, C.G., Rhee, J., Brose, N., and Papadopoulos, T. (2021). The α3
1064 subunit of GABA(A) receptors promotes formation of inhibitory synapses in the absence of
1065 collybistin. J Biol Chem *296*, 100709.
1066 Watanabe, S., Mamer, L.E., Raychaudhuri, S., Luvsanjav, D., Eisen, J., Trimbuch, T., Sohl-Kielczynski,
1067 B., Fenske, P., Milosevic, I., Rosenmund, C.*, et al.* (2018). Synaptojanin and Endophilin Mediate Neck
1068 Formation during Ultrafast Endocytosis. Neuron *98*, 1184-1197 e1186.
1069 Yang, Y., Chen, J., Chen, X., Li, D., He, J., Wang, S., Zhao, S., Yang, X., Deng, S., Tong, C.*, et al.* (2021).
1070 Endophilin A1 drives acute structural plasticity of dendritic spines in response to Ca2+/calmodulin.
1071 The Journal of cell biology *220*.
1072 Yang, Y., Chen, J., Guo, Z., Deng, S., Du, X., Zhu, S., Ye, C., Shi, Y.S., and Liu, J.J. (2018). Endophilin
1073 A1 Promotes Actin Polymerization in Dendritic Spines Required for Synaptic Potentiation. Frontiers
1074 in molecular neuroscience *11*, 177.
1075 Yang, Y., Wei, M., Xiong, Y., Du, X., Zhu, S., Yang, L., Zhang, C., and Liu, J.J. (2015). Endophilin A1
1076 regulates dendritic spine morphogenesis and stability through interaction with p140Cap. Cell
1077 research *25*, 496-516.
1078 Yu, Q., Wang, Y., Du, F., Yan, S., Hu, G., Origlia, N., Rutigliano, G., Sun, Q., Yu, H., Ainge, J.*, et al.*
1079 (2018a). Overexpression of endophilin A1 exacerbates synaptic alterations in a mouse model of
1080 Alzheimer's disease. Nature communications *9*, 2968.
1081 Yu, X., Xu, T., Ou, S., Yuan, J., Deng, J., Li, R., Yang, J., Liu, X., Li, Q., and Chen, Y. (2018b). Endophilin
1082 A1 mediates seizure activity via regulation of AMPARs in a PTZ-kindled epileptic mouse model.
1083 Experimental neurology *304*, 41-57.
1084

1085 **Figure legends**

1086

1087 **Figure 1. Ablation of endophilin A1 in CA1 neurons disrupts the E/I balance and increases**
1088 **epilepsy susceptibility.**

1089 **(A)** Experimental protocol of PTZ kindling. Saline serves as negative control for PTZ.

1090 **(B)** Representative images of convulsive behavior in each group.

1091 **(C)** Seizures were monitored and scored after each injection. Nine 10-week-old mice were used
1092 in each condition. Seizure scores are shown as means ± S.E.M. Statistical test: repeated
1093 measures ANOVA followed by Tukey post-hoc test at each time point. * $p < 0.05$, ** $p < 0.01$,
1094 *** $p < 0.001$, *EndoA1*$^{-/-}$_PTZ *vs EndoA1*$^{+/+}$_PTZ at each time point.

1095 **(D)** The representative mCherry-positive hippocampal CA1 neuron used for
1096 electrophysiological recording.

1097 **(E-F)** Representative traces of evoked excitatory postsynaptic currents (eEPSC) and
1098 quantification of mean eEPSC amplitude (E), and paired-pulse recording (F) from 10 control
1099 (Ctrl, uninfected) and 10 *EndoA1* KO (mCherry and Cre) pyramidal neurons of 4 independent
1100 animals.

1101 **(G-H)** Representative traces of evoked inhibitory postsynaptic currents (eIPSCs) and
1102 quantification of mean eIPSC amplitude (G), and paired-pulse recording (H) from 9 control and
1103 9 *EndoA1* KO pyramidal neurons of 4 independent animals.

1104 **(I)** Effect of *EndoA1* KO on the E/I ratio from 9 control and 9 *EndoA1* KO pyramidal neurons
1105 of 4 independent animals.

1106 **(J)** Representative recordings of miniature excitatory postsynaptic currents (mEPSCs) traces
1107 (+10 mV) from control or *EndoA1* KO CA1 pyramidal cells.

1108 **(K)** Cumulative probability and quantification of mEPSC amplitude from 7 control and 7
1109 *EndoA1* KO pyramidal neurons of 3 independent animals.

1110 **(L)** Cumulative probability and quantification of mEPSC frequency from 7 control and 7
1111 *EndoA1* KO pyramidal neurons of 3 independent animals.

1112 **(M)** Representative recordings of miniature inhibitory postsynaptic currents (mIPSCs) traces
1113 (–70 mV) from control or *EndoA1* KO CA1 pyramidal cells.

1114 **(N)** Cumulative probability and quantification of mIPSC amplitude from 7 control and 7
1115 *EndoA1* KO pyramidal neurons of 3 independent animals.

1116 **(O)** Cumulative probability and quantification of mIPSC frequency from 7 control and 7
1117 *EndoA1* KO pyramidal neurons of 3 independent animals. Statistical test: two-tailed Student's
1118 t-test in E-I & K, L, N, O. ns, non-significant. All data shown are scatterplots with means ±
1119 S.E.M.

1120

1121 **Figure 2. *EndoA1* KO causes defects in the formation and stabilization of inhibitory**
1122 **synapses.**

1123 **(A-B)** Immunofluorescence staining and confocal microscopy of gephyrin (GPN) in the
1124 hippocampal region of 3-week-old (P21) and 10-week-old (P60) *EndoA1*$^{+/+}$ or *EndoA1*$^{-/-}$ mouse
1125 brains. Scale bar, 50 μm.
1126 **(C)** Quantification of the signal intensity of GPN in (A) and (B). n = 6 mice for each genotype.
1127 **(D-E)** Same as (A-B) except that slices were immunostained for VGAT, (D) for P21, (E) for
1128 P60. Scale bar, 50 μm.
1129 **(F)** Quantification of VGAT signal intensity in (D) and (E). n = 6 mice for each genotype.
1130 **(G-H)** Same as (A-B) except that slices were immunostained for $GABA_AR$ γ2 (γ2). (G) for P21,
1131 (H) for P60. Scale bar, 50 μm.
1132 **(I)** Quantification of γ2 signal intensity in (G) and (H). n = 6 mice for each genotype. Statistical
1133 test: unpaired two-tailed Student's t-test. ns, non-significant. All data are scatterplots with
1134 means ± S.E.M. Abbreviations: CA1-3, cornus ammonis region 1-3; DG, dentate gyrus; DAPI
1135 staining of cell nuclei is shown in blue.
1136
1137 **Figure 3. Endophilin A1 is distributed in the iPSD and regulates the assembly of the**
1138 **inhibitory postsynaptic machinery.**
1139 **(A)** Cultured *EndoA1*$^{fl/fl}$ hippocampal neurons were transfected with construct expressing GFP
1140 or GFP-2A-Cre on DIV12, fixed and immunostained for surface GluA1 (sGluA1) or $GABA_AR$
1141 γ2 (sγ2) on DIV16. Shown are representative confocal microscopy images. Lower panels are
1142 magnification of boxed regions in the upper panels. Scale bar, 10 μm in the upper panels and 5
1143 μm in the lower panels.
1144 **(B)** Quantification of the signal intensity (left) and cluster number (right) of GPN puncta in
1145 dendrites in (A). GFP: 15 neurons; Cre: 18 neurons, from 3 independent cultures. Statistical
1146 test: unpaired two-tailed Student's t-test. ns, non-significant.
1147 **(C-D)** Cultured *EndoA1*$^{fl/fl}$ hippocampal neurons were co-transfected with constructs for GFP
1148 or GFP-2A-Cre and Flag vector or Flag-endophilin A1 (Flag-EndoA1) on DIV12, and
1149 immunostained for surface γ2 on DIV16. Shown are representative confocal images (C) and
1150 quantification of surface γ2 in dendrites (D). Scale bar, 2 μm. GFP: 18 neurons; Cre: 19 neurons;
1151 Cre + EndoA1: 18 neurons, from 3 independent cultures. Statistical test: one-way ANOVA by
1152 Tukey post hoc test.
1153 **(E-F)** *EndoA1*$^{fl/fl}$ hippocampal neurons were infected with adeno-associated virus (AAV)
1154 carrying mCherry or mCherry-2A-Cre on DIV3 and surface biotinylated on DIV16. Total and
1155 surface proteins were detected by SDS-PAGE and immunoblotting. N = 3. Statistical test:
1156 unpaired two-tailed t-test.
1157 **(G)** Hippocampal neurons were transfected with construct expressing GFP to label neuronal
1158 morphology on DIV12, then immunostained with antibodies against EndoA1 and GPN on
1159 DIV16. Shown are representative z stack maximum projection images captured by structured
1160 illumination microscopy (SIM). Lower panels are insets of boxed regions in the upper panel.

1161 Dendrites and spines are outlined in white. Scale bars, 2 μm in upper panels and 0.5 μm in
1162 magnified images.
1163 **(H)** Same as (G) except that neurons were immunostained for EndoA1 and surface γ2.
1164 **(I)** Same as (G) except that neurons were immunostained for EndoA1 and VGAT.
1165 **(J)** Immunoisolation from the membrane fraction of mouse brain tissues with antibodies against
1166 $GABA_AR$ α1 (α1) or EndoA1.
1167 **(K)** Immunoisolation from *EndoA1*$^{+/+}$ and *EndoA1*$^{-/-}$ brain lysates with antibodies to $GABA_AR$
1168 α1. Shown are representative immunoblot (left) and quantification of neuroligin 2 (NL2), GPN
1169 and $GABA_AR$ γ2 co-immunoisolated with α1 (right). N = 6 independent experiments. Statistical
1170 test: unpaired two-tailed Student's t-test.
1171 **(L)** PSD fractions were isolated by differential centrifugation from mouse brain lysates and
1172 analyzed by immunoblotting with antibodies to EndoA1 and synaptic proteins. S1,
1173 homogenates; PSD, postsynaptic density. SYP, synaptophysin. N = 7 independent experiments.
1174 Statistical test: unpaired two-tailed Student's t-test. All data represent scatter plots with means
1175 ± S.E.M.
1176
1177 **Figure 4. Endophilin A1 interacts with gephyrin and promotes its clustering in**
1178 **postsynaptic neurons.**
1179 **(A)** Silver staining of proteins co-immunoprecipitated from *EndoA1*$^{+/+}$ mouse brain lysates with
1180 antibodies to endophilin A1.
1181 **(B)** Gene Ontology (GO) enrichment analysis of EndoA1-interacting proteins identified by
1182 mass spectrometry.
1183 **(C-D)** HEK293T cells co-transfected with constructs expressing Myc-tagged GPN or HA-
1184 tagged NL2 and Flag-tagged EndoA1 for 48 h were lysed for Flag IP. Input and bound proteins
1185 were analyzed by immunoblotting with antibodies against Myc, HA and Flag.
1186 **(E)** Co-IP from brain lysates with antibodies to EndoA1.
1187 **(F)** HEK293T cells overexpressing Flag-tagged endophilin As and Myc-tagged GPN were
1188 lysed for co-immunoprecipitation.
1189 **(G)** *EndoA1*$^{fl/fl}$ hippocampal neurons were co-transfected with constructs expressing GFP and
1190 Flag vector, or GFP-2A-Cre and Flag vector, Flag-EndoA1, Flag-EndoA2 or Flag-EndoA3 on
1191 DIV12, fixed on DIV16 and immunostained for GPN, GFP and Flag. Shown are representative
1192 confocal microscopy images. Scale bar, 2 μm.
1193 (**H**) Quantification of GPN signal intensity (left) and cluster number (right) in dendrites in (G).
1194 36 neurons for GFP + vector; 34 neurons for Cre + vector; 38 neurons for Cre + EndoA1; 29
1195 neurons for Cre + EndoA2; 27 neurons for Cre + EndoA3, from 3 independent cultures.
1196 Statistical test: one-way ANOVA by Tukey post hoc test.
1197 **(I)** Hippocampal neurons were co-transfected with constructs expressing GFP and vector or
1198 Flag-EndoA1 on DIV12, fixed and immunostained for GPN on DIV16. Shown are

representative confocal microscopy images of GPN in the soma (left) and dendrites (right). Scale bars, 5 μm in the upper panels and 2 μm in the lower panels.

(J) Quantification of GPN signal intensity (left) and cluster number (right) in the soma and dendrites. 34 neurons for GFP + vector; 37 neurons for GFP + EndoA1, from 3 independent cultures. Statistical test: unpaired Student's two-tailed t-test. All data represent scatterplots with means ± S.E.M.

Figure 5. Both BAR and SH3 domains are required for endophilin A1-mediated organization of iPSD.

(A) *EndoA1*$^{fl/fl}$ hippocampal neurons expressing GFP or Cre were immunostained for GPN, surface γ2 and GFP on DIV16. Shown are representative confocal microscopy images. Scale bars, 5 μm in left panels and 1 μm in magnified images.

(B-C) Quantification of the mean intensity of GPN (green) and surface γ2 (red) and their colocalization in (A). 21 neurons for GFP, 22 neurons for Cre, from 3 independent cultures. Statistical test: unpaired two-tailed Student's t-test. All data represent scatterplots with means ± S.E.M.

(D) DIV12 hippocampal neurons were co-transfected with constructs expressing GFP and vector or Flag-EndoA1, fixed on DIV16 and immunostained for surface γ2. Shown are representative confocal microscopy images of surface γ2 in the soma (left) and dendrites (right). Scale bars, 5 μm in the upper panels and 2 μm in the lower panels.

(E) Quantification of surface γ2 mean intensity (left) and cluster number (right) in the soma and dendrites. Soma: 20 neurons for GFP + vector, 20 neurons for GFP + EndoA1; Dendrites: 35 neurons for GFP + vector, 30 neurons for GFP + EndoA1, from 3 independent cultures. Statistical test: unpaired two-tailed Student's t-test. All data represent scatterplots with means ± S.E.M.

(F) Schematic representation of EndoA1 and GPN domain structure and diagrams of fragments used for interaction mapping.

(G) GST-tagged EndoA1 fragments conjugated to Glutathione-Sepharose beads were incubated with lysates of HEK293T cells overexpressing Myc-tagged GPN. Input and bound proteins were analyzed by immunoblotting with antibodies against Myc. Bottom panel: Coomassie blue-stained SDS-PAGE gel showing GST fusion proteins. FL, full length.

(H) HEK293T cells co-transfected with constructs encoding Myc-tagged GPN and Flag-tagged EndoA1 fragments were lysed for Flag IP. Input and bound proteins were analyzed by immunoblotting with antibodies against Myc and Flag.

(I) Binding of His-tagged EndoA1 to GST-tagged GPN fragments in pull-down assay. Bound proteins were analyzed by SDS-PAGE and immunoblotting with anti-His antibodies. Input and bound proteins were analyzed by immunoblotting with antibodies against His. Bottom panel: Coomassie blue-stained SDS-PAGE gel showing GST fusion proteins. FL, full length. Right

panel: Quantification of EndoA1 binding to GPN domain. N = 3 independent experiments. Statistical test: one-way ANOVA by Tukey post hoc test. All data represent scatterplots with means ± S.E.M.

(J) DIV12 *EndoA1*$^{fl/fl}$ hippocampal neurons were co-transfected with constructs expressing GFP and Flag vector or GFP-2A-Cre, and Flag vector or Flag-EndoA1 FL, Flag-EndoA1 ΔSH3, Flag-EndoA1 aa172-352, fixed and immunostained for GPN on DIV16. Shown are representative confocal microscopy images of GPN. Scale bar, 2 μm.

(K) Quantification of mean intensity (left) and cluster number (right) in dendrites are shown for GPN in (J). 41 neurons for GFP + vector; 44 neurons for Cre + vector; 35 neurons for Cre + FL; 24 neurons for Cre + ΔSH3; 27 neurons for Cre + aa172-352, from 3 independent cultures. Statistical test: one-way ANOVA by Tukey post hoc test. All data represent scatterplots with means ± S.E.M.

(L) Same as (I) except that neurons were immunostained for surface γ2. Scale bar, 2 μm.

(M) Quantification of mean intensity (left) and cluster number (right) in dendrites are shown for surface γ2 in (K). 38 neurons for GFP + vector; 31 neurons for Cre + vector; 26 neurons for Cre + FL; 33 neurons for Cre + ΔSH3; 36 neurons for Cre + aa172-352, from 3 independent cultures. Statistical test: one-way ANOVA by Tukey post hoc test. All data represent scatterplots with means ± S.E.M.

Figure 6. Actin polymerization is required for stabilization of inhibitory postsynapses.

(A-D) DIV12 cultured hippocampal neurons transiently expressing GFP were treated with DMSO (vehicle control), 1 μM Latrunculin A (LatA) or 1 μM Nocodazole (Noco) for 60 min (A) or 120 min (C) on DIV16, respectively. Changes in postsynaptic proteins GPN (red) and PSD95 (green) were detected by confocal microscopy. Quantitative data shown were the mean intensity (left) and cluster number (right) of GPN and PSD95 at 60 min (B) and 120 min (D). Ctrl: 20 neurons for 60 min; 29 neurons for 120 min; LatA: 20 neurons for 60 min; 33 neurons for 120 min; Noco: 23 neurons for 60 min; 22 neurons for 120 min, from 3 independent cultures. Statistical test: one-way ANOVA by Tukey post hoc test. Scale bar, 5 μm.

(E-H) Same as (A-D) except that neurons were immunostained for GPN (red) and surface γ2 (green). Changes in GPN and surface γ2 at 60 min (E) or 120 min (G) were detected by confocal microscopy. Quantitative data shown were the mean intensity (left) and cluster number (right) of GPN and surface γ2 at 60 min (F) and 120 min (H). Ctrl: 35 neurons for 60 min; 24 neurons for 120 min; LatA: 34 neurons for 60 min; 20 neurons for 120 min; Noco: 34 neurons for 60 min; 24 neurons for 120 min, from 3 independent cultures. Statistical test: one-way ANOVA by Tukey post hoc test. Scale bar, 5 μm.

(I) Levels of synaptic proteins normalized to control neurons following LatA or Noco treatment in (A,C,E,G).

(J-K) The colocalization between surface γ2 and GPN signals in dendrites in (E) and (G). Statistical test: one-way ANOVA by Tukey post hoc test. All data are scatterplots with means ± S.E.M.

Figure 7. Both the membrane-binding and p140Cap-binding capacities of endophilin A1 are required for iPSD assembly and E/I balance.

(A) Cultured hippocampal neurons from *EndoA1*$^{fl/fl}$ mice were co-transfected with construct expressing GFP and Flag vector or GFP-2A-Cre and Flag vector, Flag-EndoA1 wild-type (WT), mutants (KKK-EEE or Y343A) or p140Cap, and analyzed on DIV16 by immunofluorescence staining for GPN (green) and GFP (red). Scale bar, 2 μm.

(B) Quantification of GPN mean intensity (left) and cluster number (right) in (A). 35 neurons for GFP vector; 43 neurons for Cre + vector; 32 neurons for Cre + WT; 33 neurons for Cre + KKK-EEE; 36 neurons for Cre + Y343A; 33 neurons for Cre + p140Cap, from 3 independent cultures. Statistical test: one-way ANOVA by Tukey post hoc test.

(C) Same as (A) except that neurons were immunostained for surface γ2 on DIV16. Scale bar, 2 μm.

(D) Quantification of surface γ2 mean intensity (left) and number (right) in (C). 44 neurons for GFP + vector; 42 neurons for Cre + vector; 32 neurons for Cre + WT; 35 neurons for Cre + KKK-EEE; 35 neurons for Cre + Y343A; 32 neurons for Cre + p140Cap, from 3 independent cultures. Statistical test: one-way ANOVA by Tukey post hoc test.

(E) Experimental scheme for seizure scoring of *EndoA1*$^{fl/fl}$ mice stereotactically co-injected with AAVs carrying mCherry and Cre, and EGFP and EndoA1 or its mutants (KKK-EEE and Y343A) in the hippocampal CA1 region. Mice were intraperitoneally administered PTZ for 12 days after AAV injections, then seizures were scored.

(F) PTZ-induced seizures in mice injected with the indicated AAVs were scored for 30 min. Ctrl, 7 mice; Cre, 7 mice; Cre + WT, 7 mice; Cre + KKK-EEE, 6 mice; Cre + Y343A, 7 mice.; Statistical test: repeated measures ANOVA followed by Tukey post-hoc test at each time point. * $p < 0.05$, ** $p < 0.01$, *** $p < 0.001$, red color is for Cre *vs* Ctrl, green color is for Cre + WT *vs* Cre. All data are means ± S.E.M.

(G-K) AAVs expressing Cre (AAV-mCherry-2A-Cre) and GFP (AAV-EGFP) or Cre and EndoA1 WT or mutant (AAV-EGFP-2A-EndoA1, AAV-EGFP-2A-EndoA1 KKK-EEE, AAV-EGFP-2A-EndoA1 Y343A) were stereotaxically injected into the CA1 regions of *EndoA1*$^{fl/fl}$ mouse brain at P0. Acute hippocampal slices were prepared on P14-P21 for dual recording of evoked excitatory postsynaptic currents (eEPSC) and inhibitory postsynaptic currents (eIPSC). Shown are representative traces and pairwise comparisons of noninfected (Ctrl) and infected neurons in the same slice. Scale bar = 50/50, 50/50, 50/50, 50/50, 40/20 (pA/ms) in (G); Scale bar = 100/100, 100/400, 100/100, 100/200, 300/100 (pA/ms) in (H); Scale bar = 50/50, 50/50, 50/50, 50/50, 50/50 (pA/ms) in (I); Scale bar = 100/100, 200/100, 100/100, 100/200, 100/200 (pA/ms) in (J). Statistical test: unpaired two-tailed Student's t-test. ns, non-significant; All data are scatterplots with means ± S.E.M. All number of recording were from more than 7 pyramidal neurons of 3 independent animals.

1315

1316 **Figure 8. Model for the role of endophilin A1 at the inhibitory postsynapses and E/I**
1317 **balance.**
1318 **(A)** Endophilin A1 directly interacts with the inhibitory postsynaptic scaffold protein gephyrin
1319 to promote organization of iPSD and synaptic recruitment/stabilization of the $GABA_A$Rs via its
1320 plasma membrane association and actin polymerization-promoting activities. **(B)** Loss of
1321 endophilin A1 impairs inhibitory synaptic neurotransmission and disrupts the balance of
1322 excitatory/inhibitory activities in the neural circuits, leading to enhanced epileptic seizure
1323 susceptibility.

1324 **Figure S1. Loss of endophilin A1 *in vivo* does not affect fast mIPSCs (perisomatic events:**
1325 **< 2.8 ms) and slow mIPSCs (distal dendritic events: >2.8 ms). Related to Figure 1**
1326 **(A)** Quantification of somatic and dendritic amplitudes in Ctrl and *EndoA1* KO neuron. n = 7
1327 Ctrl and 9 *EndoA1* KO neurons from 3 independent mice. Data are scatterplots with mean ±
1328 S.E.M.
1329 **(B)** Frequency of somatic and dendritic events from Ctrl and *EndoA1* KO mice. Ctrl: 7 neurons;
1330 *EndoA1* KO: 9 neurons from 3 independent mice. Data are scatterplots with mean ± S.E.M.
1331

1332 **Figure S2. Effects of *EndoA1* knockout on excitatory and inhibitory synapses in the**
1333 **hippocampus. Related to Figure 2**
1334 **(A-B)** Immunofluorescence analysis of PSD95 clusters in the hippocampal region of 3-week-
1335 old (P21) (left) and 10-week-old (P60) (right) $EndoA1^{+/+}$ and $EndoA1^{-/-}$ mouse brains. Scale
1336 bar, 50 μm.
1337 **(C)** Quantification of the mean intensity of PSD95 in the hippocampal region of 3-week-old
1338 (P21) and 10-week-old (P60) $EndoA1^{+/+}$ and $EndoA1^{-/-}$ mouse brains. n = 6 mice for each
1339 genotype. Statistical test: unpaired two-tailed Student's t-test. Data are scatterplots with mean
1340 ± S.E.M.
1341 **(D-E)** Immunofluorescent signals of VGLUT1 in the hippocampal region of 3-week-old (P21)
1342 (left) and 10-week-old (P60) (right) $EndoA1^{+/+}$ and $EndoA1^{-/-}$ mouse brains. Scale bar, 50 μm.
1343 **(F)** Quantification of the mean intensity of VGLUT1 in the hippocampal region of 3-week-old
1344 (P21) and 10-week-old (P60) $EndoA1^{+/+}$ and $EndoA1^{-/-}$ mouse brains. n = 6 mice for each
1345 genotype. Statistical test: unpaired two-tailed Student's t-test. Data are scatterplots with mean
1346 ± S.E.M.
1347 **(G)** Immunofluorescent signals of GPN in distinct layers of P60 mouse hippocampus. Scale bar,
1348 50 μm.
1349 **(H)** Quantification of gephyrin (GPN) mean intensity in distinct layers of hippocampus. n = 6
1350 mice for each genotype. Abbreviations: CA1-3, cornus Ammonis region 1-3; DG, dentate gyrus;
1351 slm, stratum lacunosum-moleculare; so, stratum oriens; sp, stratum pyramidal; sr, stratum
1352 radiatum. DAPI staining of cell nuclei is shown in blue. Statistical test: two-tailed Student's t-

test. ns, non-significant. Data are scatterplots with mean ± S.E.M.

Figure S3. Changes of endogenous postsynaptic proteins visualized by recombinant probes after depletion of EndoA1. Related to Figure 4

(A) AAVs expressing GFP (AAV-GFP) or GFP and Cre (AAV-GFP-2A-Cre) and mRuby2-GPN.FingR were stereotaxically injected into the CA1 regions of *EndoA1*$^{fl/fl}$ mouse brain at P0. Brain sections from P21 mice were fixed and immunostained for GFP and mRuby. Representative images at 40× magnification with 4× digital zoom showed the expression patterns of mRuby2-GPN.FingR. Scale bars, 10 μm.

(B) Quantification of signal intensity of mRuby2-GPN.FingR in (C). n = 8 mice for each genotype.

(C) AAVs expressing mCherry (AAV-mCherry) or mCherry and Cre (AAV-mCherry-2A-Cre) and PSD95.FingR-eGFP were stereotaxically injected into the CA1 regions of *EndoA1*$^{fl/fl}$ mouse brain at P0. Brain sections from P21 mice were fixed and immunostained for mCherry and GFP. Representative images at 40× magnification with 4× digital zoom showed the expression patterns of PSD95.FingR-eGFP. Scale bars, 10 μm.

(D) Quantification of signal intensity of PSD95.FingR-eGFP in (A). n = 6 mice for each genotype.

Figure S4. Expression of GABA$_A$R α1 in cultured hippocampal neurons and the localization of EndoA1 in inhibitory pre- and postsynaptic sites. Related to Figure 3

(A) Cultured hippocampal neurons were fixed on DIV16 and immunostained for surface GABA$_A$R α1. Shown are representative confocal microscopy images. Scale bar, 10 μm.

(B) Hippocampal neurons were fixed and immunostained with antibodies against EndoA1, Bassoon and GPN on DIV16. Shown are representative z stack maximum projection images captured by structured illumination microscopy (SIM). Lower panels are insets of boxed regions in the upper panel. Lower panels are insets of boxed regions in the upper panel. Scale bars, 5 μm in upper panels and 0.5 μm in magnified images.

(C-D) Color composite of the two input images (left) and composite image of the data that contributed to the Gaussian result (right) for spatial colocalization analysis in super-resolutional images. Scale bars, 5 μm.

(E-F) The blue line is the radial profle of original cross-correlation, the green line is the radial profle after the pixel randomization procedure, and the red dashed line is the fit Gaussian curve. CCC generates four statistical parameters (μ (the mean distance of the measured spatial correlation), σ (standard deviation distance for the spatial correlation), Confidence and R-squared) that was used to evaluate spatial correlation of GPN and EndoA1 in (E), and of Bassoon and EndoA1 in (F).

(G) The ratio of GPN or Bassoon cross-correlated with EndoA1 to total GPN or Bassoon,

respectively. n = 14, from 3 independent cultures. All data are scatterplots with means ± S.E.M.

Figure S5. Effect of *EndoA1* knockout on gephyrin clustering in cultured hippocampal neurons. Related to Figure 4

(A) *EndoA1*$^{fl/fl}$ hippocampal neurons were co-transfected with constructs expressing mCherry and GPN.FingR-eGFP or mCherry-2A-Cre and GPN.FingR-eGFP on DIV12, then fixed and immunostained for eGFP and mCherry on DIV16. Shown are representative confocal microscopy images of GPN.FingR-eGFP. The right panels are magnification of soma or boxed regions in the left panels. Scale bar, 10 μm in the left panels and 5 μm in the right panels.

(B) Quantification of GPN.FingR-eGFP mean intensity in the soma (left), mean intensity (center) and cluster number (right) in dendrites. Scale bar, 5 μm. 20 neurons for mCherry + GPN.FingR-eGFP; 20 neurons for Cre + GPN.FingR-eGFP. Statistical test: unpaired two-tailed Student's t-test. All data are scatterplots with means ± S.E.M.

(C) Same as (E) except that neuron were co-transfected with PSD.FingR-eGFP.

(D) Quantification of PSD95.FingR-eGFP mean intensity in the soma (left), mean intensity (center) and cluster number (right) in dendrites. Scale bar, 5 μm. 14 neurons for mCherry + PSD95.FingR-eGFP; 13 neurons for Cre + PSD95.FingR-eGFP. Statistical test: unpaired two-tailed Student's t-test. All data are scatterplots with means ± S.E.M.

(E-G) *EndoA1*$^{fl/fl}$ hippocampal neurons were transfected with construct expressing mCherry or mCherry-2A-Cre on DIV12 and immunostained for GPN and mCherry on DIV16. Shown are representative confocal microscopy images for GPN in the soma, axon initial segment (AIS) and dendrites 30 μm, 60 μm, 90 μm or120 μm from the soma, respectively. Scale bars, 5 μm.

(H) Quantification of GPN mean intensity normalized to the mCherry group in the soma (A), AIS (B) and dendrites at various distances from the soma (C). Number: 40 (mCherry), 47 (Cre) for soma; 26 (mCherry), 25 (Cre) for AIS; 55 (mCherry), 52 (Cre) for dendrites 30 μm; 52 (mCherry), 50 (Cre) for dendrites 60 μm; 48 (mCherry), 47 (Cre) for dendrites 90 μm; 49 (mCherry), 41 (Cre) for dendrites 120 μm. Ankyrin-G: Axon initial segment (AIS) labeling marker. Statistical test: unpaired two-tailed Student's t-test . All data are scatterplots with means ± S.E.M for each group.

Figure S6. p140Cap promotes gephyrin clustering via endophilin A1-mediated pathway. Related to Figure 6 and 7

(A) Cultured hippocampal neurons transiently expressing GFP and LifeAct-mCherry were immunostained for GPN, GFP and mCherry on DIV16. Shown are representative z stack maximum projection images captured by structured illumination microscopy (SIM). Right panels are insets of boxed regions in the left panel. Scale bars, 2 μm in left panels and 0.5 μm in magnified images.

(B) Cultured hippocampal neurons were co-transfected with Ctrl shRNA and vector or p140Cap

shRNA and vector or RNAi-resistant Flag-tagged p140Cap on DIV 11, followed by immunostaining with antibodies to GPN, Flag (blue) and RFP on DIV 16. Scale bar, 5 μm.

(C) Quantification of GPN mean intensity and puncta number in (B). 18 neurons for shCtrl + vector; 20 neurons for shp140Cap + vector; 22 neurons for shp140Cap + p140Cap, from 3 independent cultures. Statistical test: One-way ANOVA followed by Tukey post-hoc test. All data shown are scatterplots with means ± S.E.M.

(D) *EndoA1*$^{fl/fl}$ hippocampal neurons coexpressing GFP and Ctrl shRNA or p140Cap shRNA, or GFP-2A-Cre and Ctrl shRNA or p140Cap shRNA were immunostained for GPN on DIV16. Shown are representative confocal microscopy images. Scale bar, 5 μm.

(E) Quantification of GPN mean intensity and puncta number in (D). 27 neurons for GFP + shCtrl; 26 neurons for GFP + shp140Cap; 23 neurons for Cre + shCtrl; 26 neurons for Cre + shp140Cap, from 3 independent cultures. Statistical test: One-way ANOVA followed by Tukey post-hoc test. All data shown are scatterplots with means ± S.E.M.

Table S1. Proteins identified by mass spec analysis of endophilin A1 co-immunoprecipitates and their abundance. Related to Figure 4

Video S1. PTZ kindling behaviors of *EndoA1*$^{+/+}$ and *EndoA1*$^{-/-}$ mice. Related to Figure 1

Video S2. The spatial relationship between EndoA1 and GPN. **Related to Figure 3G.** 3D-SIM movie of an enlarged region of interest (ROI) from a hippocampal neuron dendrite shows the association of EndoA1 (red) and GPN (green).

Video S3. The spatial relationship between endophilin A1 and surface GABA$_A$R γ2. **Related to Figure 3H.** 3D-SIM movie of an enlarged region of interest from a hippocampal neuron dendrite shows the association of EndoA1 (red) and surface GABA$_A$R γ2 (green).

Video S4. The spatial relationship between endophilin A1 and VGAT. **Related to Figure 3I.** 3D-SIM movie of an enlarged region of interest from a hippocampal neuron dendrite shows the signals of EndoA1 (red) and VGAT (green).

Video S5. The spatial relationship between Bassoon, gephyrin and endophilin A1. Related to Figure S3B. 3D-SIM movie of an enlarged region of interest from a hippocampal neuron dendrite shows the signals of Bassoon (blue), GPN (green) and EndoA1 (red).

Video S6. The spatial relationship between gephyrin and LifeAct. Related to Figure 6 and Figure S5A. 3D-SIM movie of an enlarged region of interest from a hippocampal neuron dendrite shows the signals of LifeAct (red) and GPN (green).

1467

1468 **Video S7. PTZ kindling behaviors of *EndoA1*$^{fl/fl}$ mice injected with AAVs expressing Cre**
1469 **and EndoA1 WT or mutants. Related to Figure 7**

1470

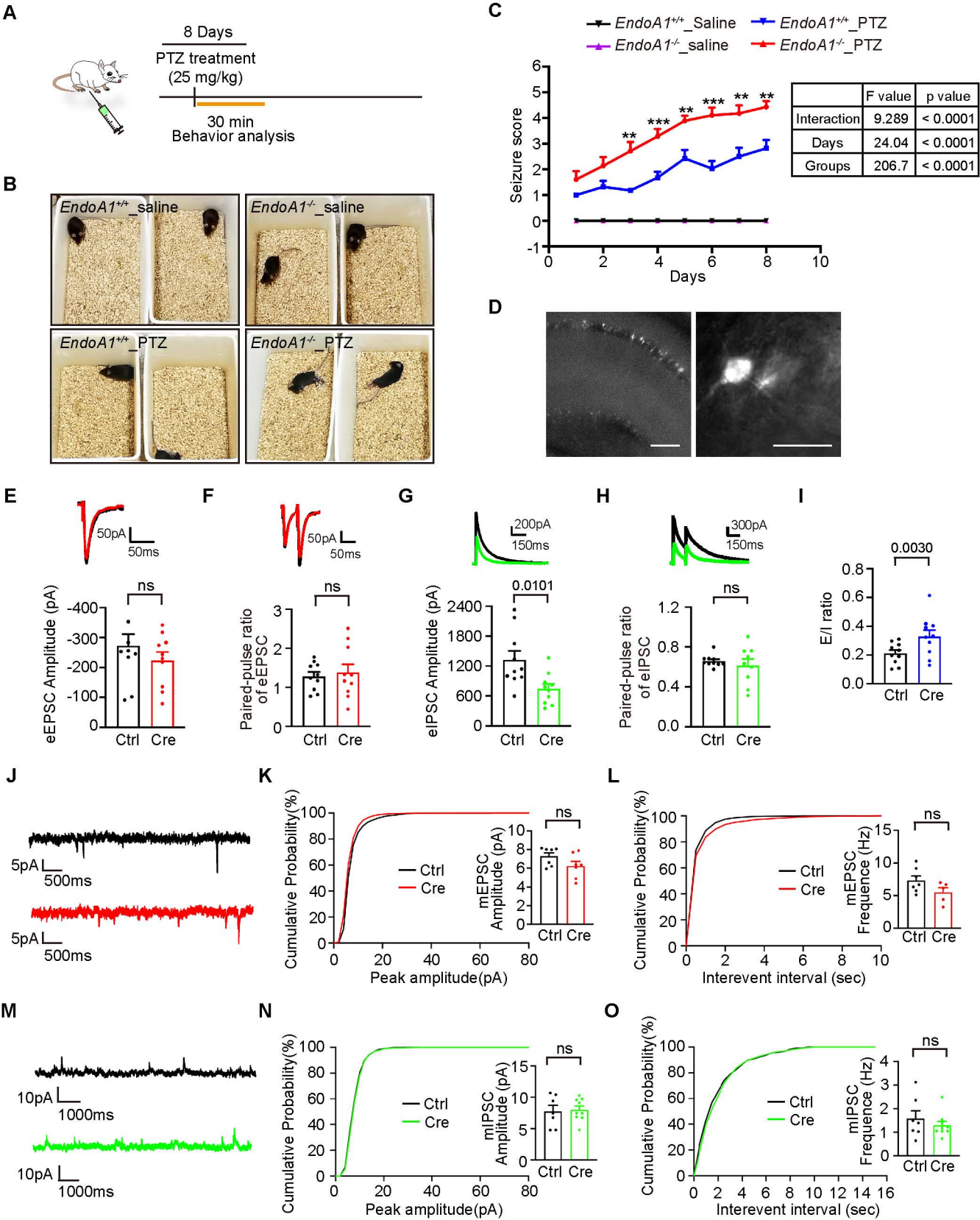
A
8 Days
PTZ treatment
(25 mg/kg)
30 min
Behavior analysis
B
EndoA1+/+_saline
EndoA1-/-_saline
EndoA1+/+_PTZ
EndoA1-/-_PTZ
C
EndoA1+/+_Saline
EndoA1+/+_PTZ
EndoA1-/-_saline
EndoA1-/-_PTZ
Seizure score
Days
F value
p value
Interaction 9.289 < 0.0001
Days 24.04 < 0.0001
Groups 206.7 < 0.0001
D
E
50pA
50ms
eEPSC Amplitude (pA)
ns
Ctrl
Cre
F
Paired-pulse ratio of eEPSC
G
200pA
150ms
eIPSC Amplitude (pA)
0.0101
H
300pA
Paired-pulse ratio of eIPSC
I
E/I ratio
0.0030
J
5pA
500ms
K
Cumulative Probability(%)
Peak amplitude(pA)
mEPSC Amplitude (pA)
L
Interevent interval (sec)
mEPSC Frequence (Hz)
M
10pA
1000ms
N
mIPSC Amplitude (pA)
O
mIPSC Frequence (Hz)

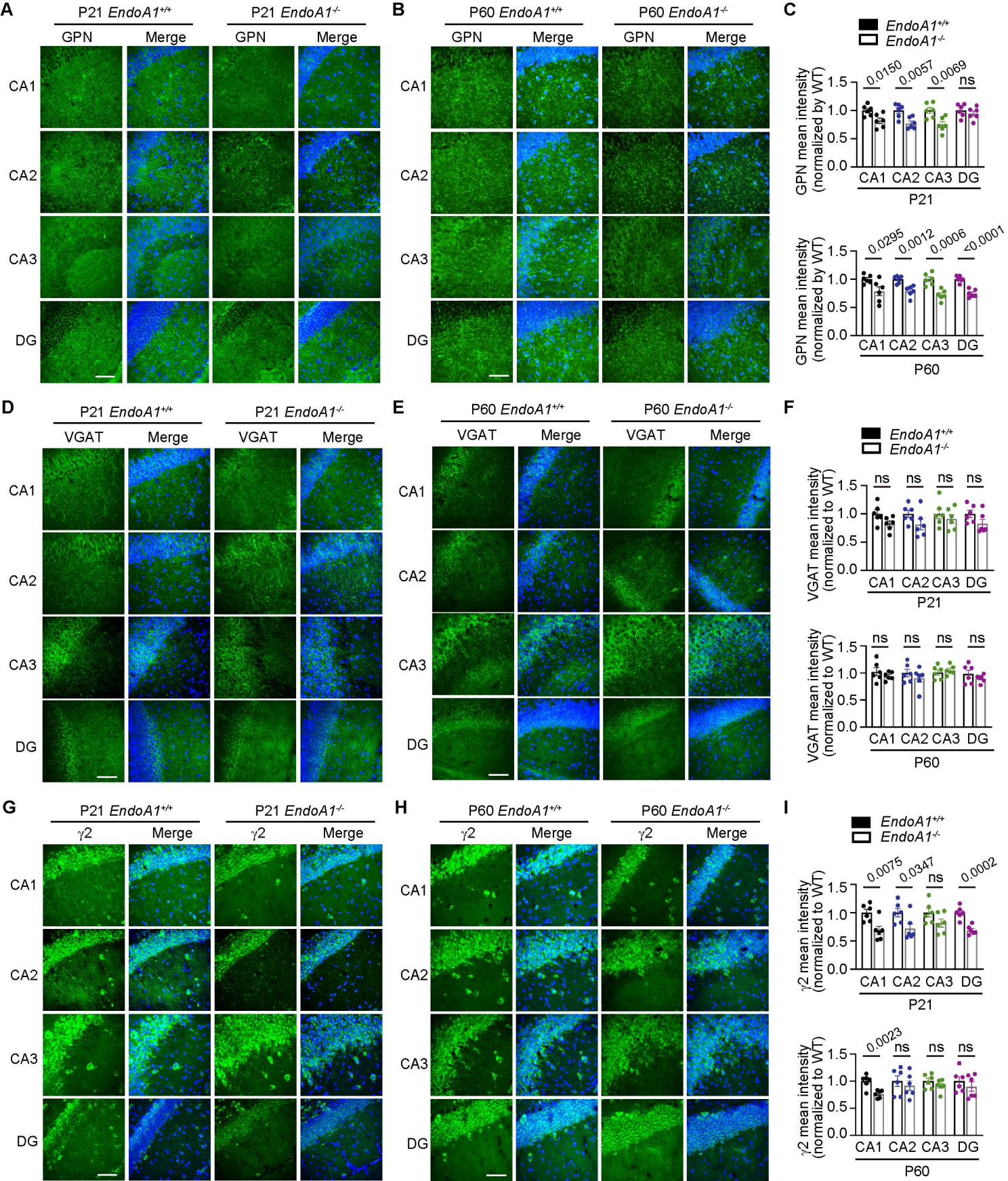
A
P21 EndoA1+/+
P21 EndoA1-/-
GPN
Merge
CA1
CA2
CA3
DG
B
P60 EndoA1+/+
P60 EndoA1-/-
C
EndoA1+/+
EndoA1-/-
GPN mean intensity (normalized by WT)
0.0150
0.0057
0.0069
ns
CA1 CA2 CA3 DG
P21
0.0295
0.0012
0.0006
<0.0001
P60
D
VGAT
E
F
VGAT mean intensity (normalized to WT)
G
γ2
H
I
γ2 mean intensity (normalized to WT)
0.0075
0.0347
0.0002
0.0023

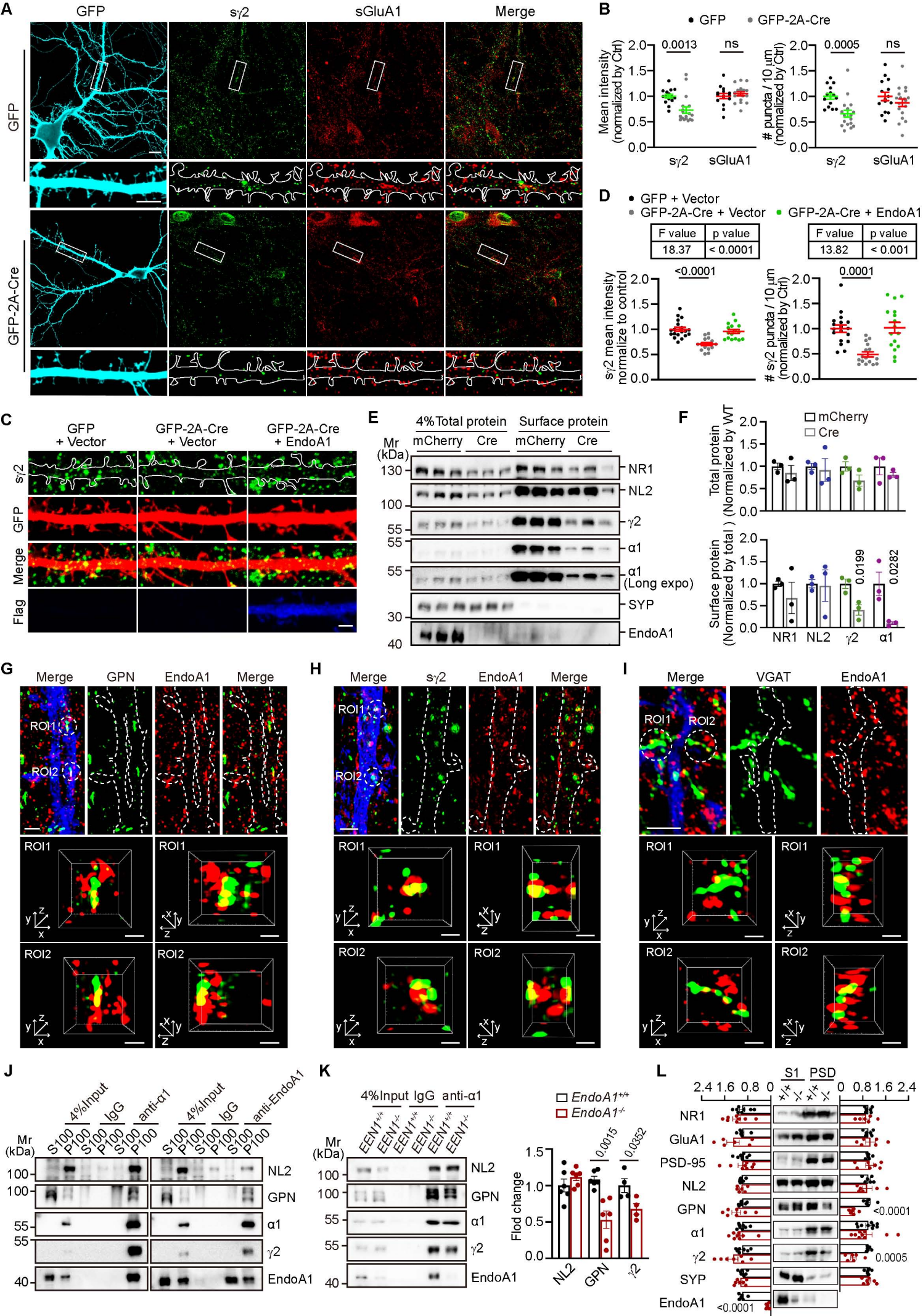
A
GFP
sγ2
sGluA1
Merge
GFP
GFP-2A-Cre
B
GFP
GFP-2A-Cre
Mean intensity (normalized by Ctrl)
puncta / 10 μm (normalized by Ctrl)
0.0013
ns
0.0005
ns
sγ2
sGluA1
D
GFP + Vector
GFP-2A-Cre + Vector
GFP-2A-Cre + EndoA1
F value
p value
18.37
< 0.0001
13.82
< 0.001
sγ2 mean intensity normalize to control
sγ2 puncta / 10 μm (normalized by Ctrl)
<0.0001
0.0001
C
GFP + Vector
GFP-2A-Cre + Vector
GFP-2A-Cre + EndoA1
sγ2
GFP
Merge
Flag
E
4%Total protein
Surface protein
mCherry
Cre
Mr (kDa)
130
100
55
55
55
30
40
NR1
NL2
γ2
α1
α1 (Long expo)
SYP
EndoA1
F
mCherry
Cre
Total protein (Normalized by WT)
Surface protein (Normalized by total)
0.0199
0.0282
NR1
NL2
γ2
α1
G
Merge
GPN
EndoA1
Merge
ROI1
ROI2
H
Merge
sγ2
EndoA1
Merge
ROI1
ROI2
I
Merge
VGAT
EndoA1
ROI1
ROI2
J
4%Input
IgG
anti-α1
anti-EndoA1
S100
P100
Mr (kDa)
100
100
55
55
40
NL2
GPN
α1
γ2
EndoA1
K
4%Input
IgG
anti-α1
EEN1+/+
EEN1-/-
Mr (kDa)
100
100
55
55
40
NL2
GPN
α1
γ2
EndoA1
EndoA1+/+
EndoA1-/-
Flod change
0.0015
0.0352
NL2
GPN
γ2
L
S1
PSD
+/+
-/-
NR1
GluA1
PSD-95
NL2
GPN
α1
γ2
SYP
EndoA1
<0.0001
0.0005
<0.0001

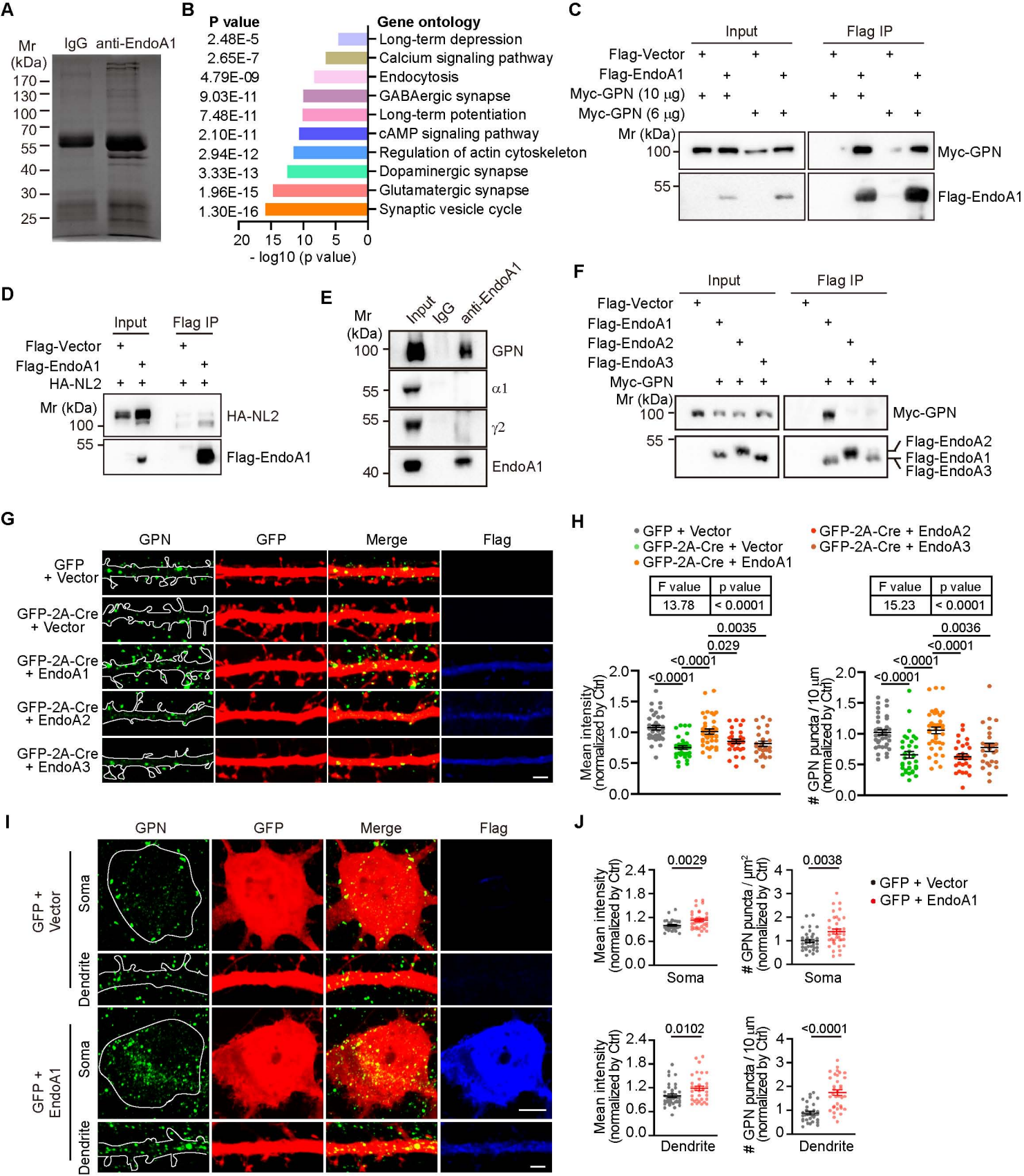
A
Mr (kDa)
IgG
anti-EndoA1
170
130
100
70
55
40
30
25
B
P value
Gene ontology
2.48E-5 Long-term depression
2.65E-7 Calcium signaling pathway
4.79E-09 Endocytosis
9.03E-11 GABAergic synapse
7.48E-11 Long-term potentiation
2.10E-11 cAMP signaling pathway
2.94E-12 Regulation of actin cytoskeleton
3.33E-13 Dopaminergic synapse
1.96E-15 Glutamatergic synapse
1.30E-16 Synaptic vesicle cycle
20 15 10 5 0
- log10 (p value)
C
Input
Flag IP
Flag-Vector
Flag-EndoA1
Myc-GPN (10 μg)
Myc-GPN (6 μg)
Mr (kDa)
100
55
Myc-GPN
Flag-EndoA1
D
Input
Flag IP
Flag-Vector
Flag-EndoA1
HA-NL2
Mr (kDa)
100
55
HA-NL2
Flag-EndoA1
E
Mr (kDa)
Input
IgG
anti-EndoA1
100
55
55
40
GPN
α1
γ2
EndoA1
F
Input
Flag IP
Flag-Vector
Flag-EndoA1
Flag-EndoA2
Flag-EndoA3
Myc-GPN
Mr (kDa)
100
55
Myc-GPN
Flag-EndoA2
Flag-EndoA1
Flag-EndoA3
G
GPN
GFP
Merge
Flag
GFP + Vector
GFP-2A-Cre + Vector
GFP-2A-Cre + EndoA1
GFP-2A-Cre + EndoA2
GFP-2A-Cre + EndoA3
H
GFP + Vector
GFP-2A-Cre + Vector
GFP-2A-Cre + EndoA1
GFP-2A-Cre + EndoA2
GFP-2A-Cre + EndoA3
F value | p value
13.78 | < 0.0001
15.23 | < 0.0001
0.0035
0.029
<0.0001
<0.0001
0.0036
<0.0001
<0.0001
<0.0001
Mean intensity (normalized by Ctrl)
GPN puncta / 10 μm (normalized by Ctrl)
2.0
1.5
1.0
0.5
0.0
I
GPN
GFP
Merge
Flag
GFP + Vector
Soma
Dendrite
GFP + EndoA1
Soma
Dendrite
J
0.0029
0.0038
0.0102
<0.0001
Mean intensity (normalized by Ctrl)
GPN puncta / μm² (normalized by Ctrl)
GPN puncta / 10 μm (normalized by Ctrl)
Soma
Dendrite
GFP + Vector
GFP + EndoA1

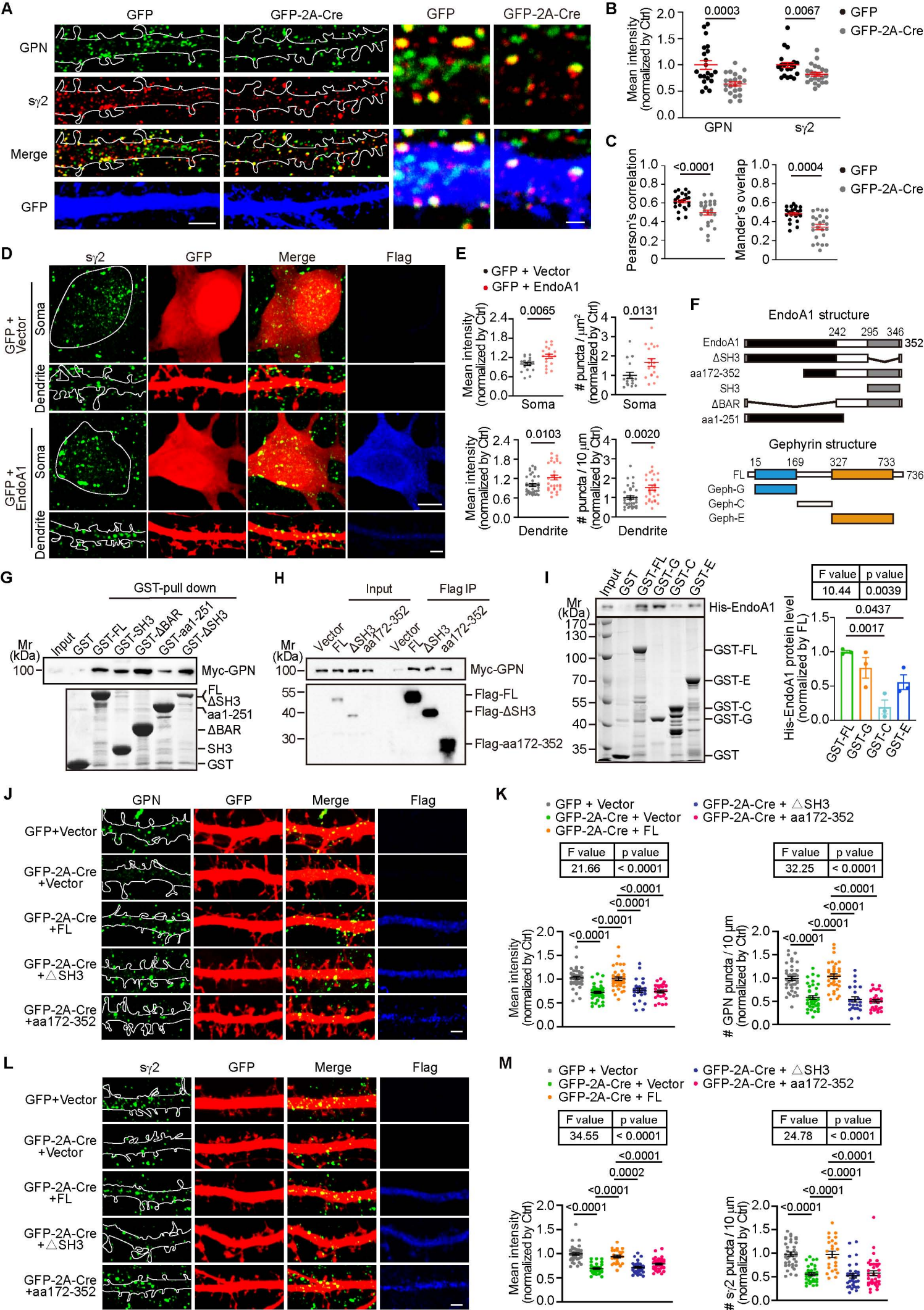
A
GFP
GFP-2A-Cre
GFP
GFP-2A-Cre
GPN
sγ2
Merge
GFP
B
Mean intensity (normalized by Ctrl)
0.0003
0.0067
GFP
GFP-2A-Cre
GPN
sγ2
C
Pearson's correlation
<0.0001
Mander's overlap
0.0004
GFP
GFP-2A-Cre
D
sγ2
GFP
Merge
Flag
GFP + Vector
Soma
Dendrite
GFP + EndoA1
Soma
Dendrite
E
GFP + Vector
GFP + EndoA1
Mean intensity (normalized by Ctrl)
0.0065
puncta / μm² (normalized by Ctrl)
0.0131
Soma
Mean intensity (normalized by Ctrl)
0.0103
puncta / 10 μm (normalized by Ctrl)
0.0020
Dendrite
F
EndoA1 structure
242
295
346
352
EndoA1
ΔSH3
aa172-352
SH3
ΔBAR
aa1-251
Gephyrin structure
15
169
327
733
736
FL
Geph-G
Geph-C
Geph-E
G
GST-pull down
Mr (kDa)
Input
GST
GST-FL
GST-SH3
GST-ΔBAR
GST-aa1-251
GST-ΔSH3
100
Myc-GPN
FL
ΔSH3
aa1-251
ΔBAR
SH3
GST
H
Input
Flag IP
Mr (kDa)
Vector
FL
ΔSH3
aa172-352
Vector
FL
ΔSH3
aa172-352
100
Myc-GPN
55
40
30
Flag-FL
Flag-ΔSH3
Flag-aa172-352
I
Input
GST
GST-FL
GST-G
GST-C
GST-E
Mr (kDa)
His-EndoA1
170
130
100
70
55
40
35
GST-FL
GST-E
GST-C
GST-G
GST
F value
p value
10.44
0.0039
0.0437
0.0017
His-EndoA1 protein level (normalized by FL)
GST-FL
GST-G
GST-C
GST-E
J
GPN
GFP
Merge
Flag
GFP+Vector
GFP-2A-Cre +Vector
GFP-2A-Cre +FL
GFP-2A-Cre +△SH3
GFP-2A-Cre +aa172-352
K
GFP + Vector
GFP-2A-Cre + Vector
GFP-2A-Cre + FL
GFP-2A-Cre + △SH3
GFP-2A-Cre + aa172-352
F value
p value
21.66
< 0.0001
F value
p value
32.25
< 0.0001
<0.0001
<0.0001
<0.0001
<0.0001
Mean intensity (normalized by Ctrl)
<0.0001
<0.0001
<0.0001
<0.0001
GPN puncta / 10 μm (normalized by Ctrl)
L
sγ2
GFP
Merge
Flag
GFP+Vector
GFP-2A-Cre +Vector
GFP-2A-Cre +FL
GFP-2A-Cre +△SH3
GFP-2A-Cre +aa172-352
M
GFP + Vector
GFP-2A-Cre + Vector
GFP-2A-Cre + FL
GFP-2A-Cre + △SH3
GFP-2A-Cre + aa172-352
F value
p value
34.55
< 0.0001
F value
p value
24.78
< 0.0001
<0.0001
0.0002
<0.0001
<0.0001
Mean intensity (normalized by Ctrl)
<0.0001
<0.0001
<0.0001
<0.0001
sγ2 puncta / 10 μm (normalized by Ctrl)

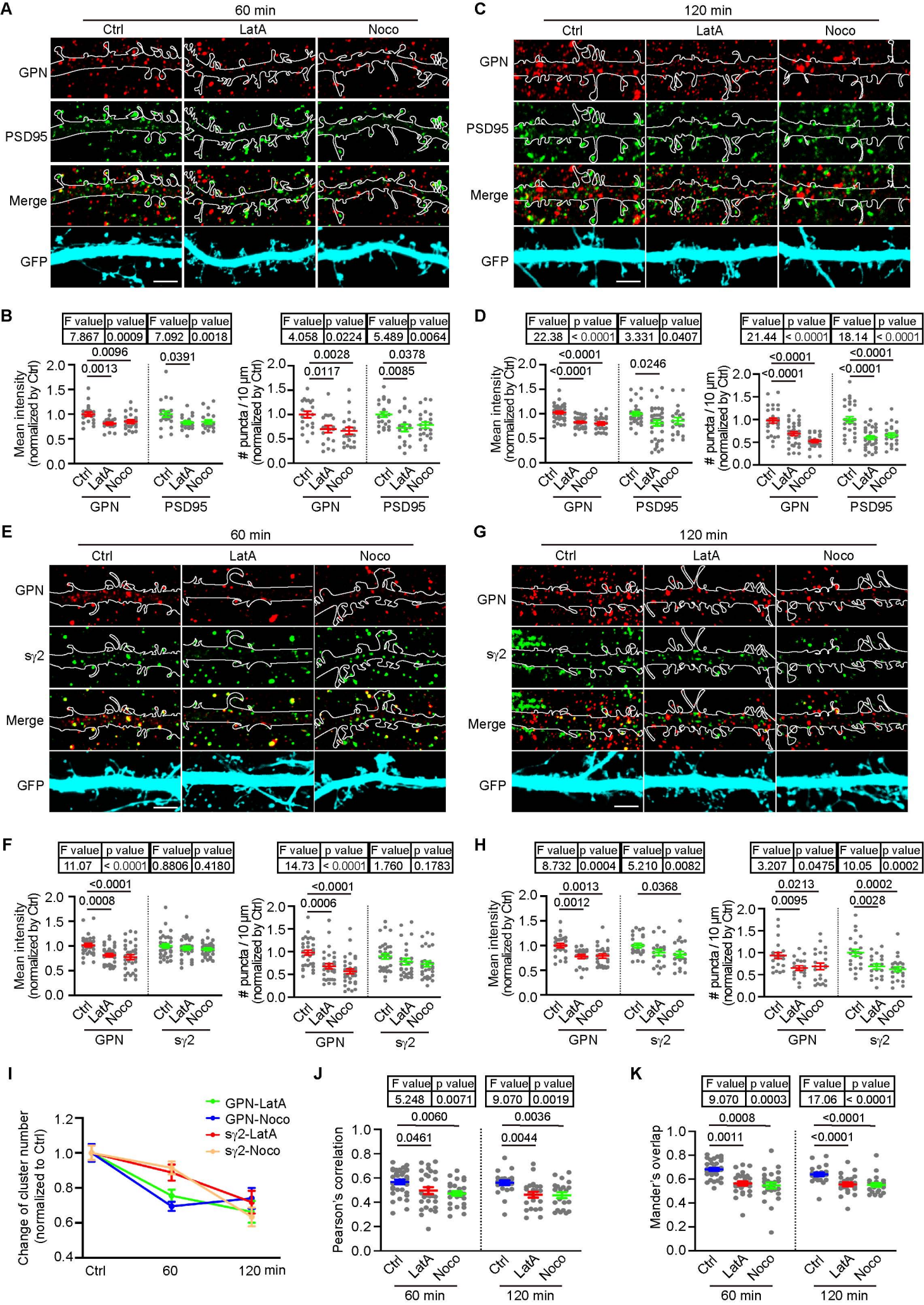
A
60 min
Ctrl
LatA
Noco
GPN
PSD95
Merge
GFP
C
120 min
B
F value | p value | F value | p value
7.867 | 0.0009 | 7.092 | 0.0018
4.058 | 0.0224 | 5.489 | 0.0064
Mean intensity (normalized by Ctrl)
puncta / 10 µm (normalized by Ctrl)
GPN
PSD95
D
22.38 | < 0.0001 | 3.331 | 0.0407
21.44 | < 0.0001 | 18.14 | < 0.0001
E
sγ2
G
F
11.07 | < 0.0001 | 0.8806 | 0.4180
14.73 | < 0.0001 | 1.760 | 0.1783
H
8.732 | 0.0004 | 5.210 | 0.0082
3.207 | 0.0475 | 10.05 | 0.0002
I
GPN-LatA
GPN-Noco
sγ2-LatA
sγ2-Noco
Change of cluster number (normalized to Ctrl)
60
120 min
J
5.248 | 0.0071
9.070 | 0.0019
Pearson's correlation
60 min
K
9.070 | 0.0003
17.06 | < 0.0001
Mander's overlap

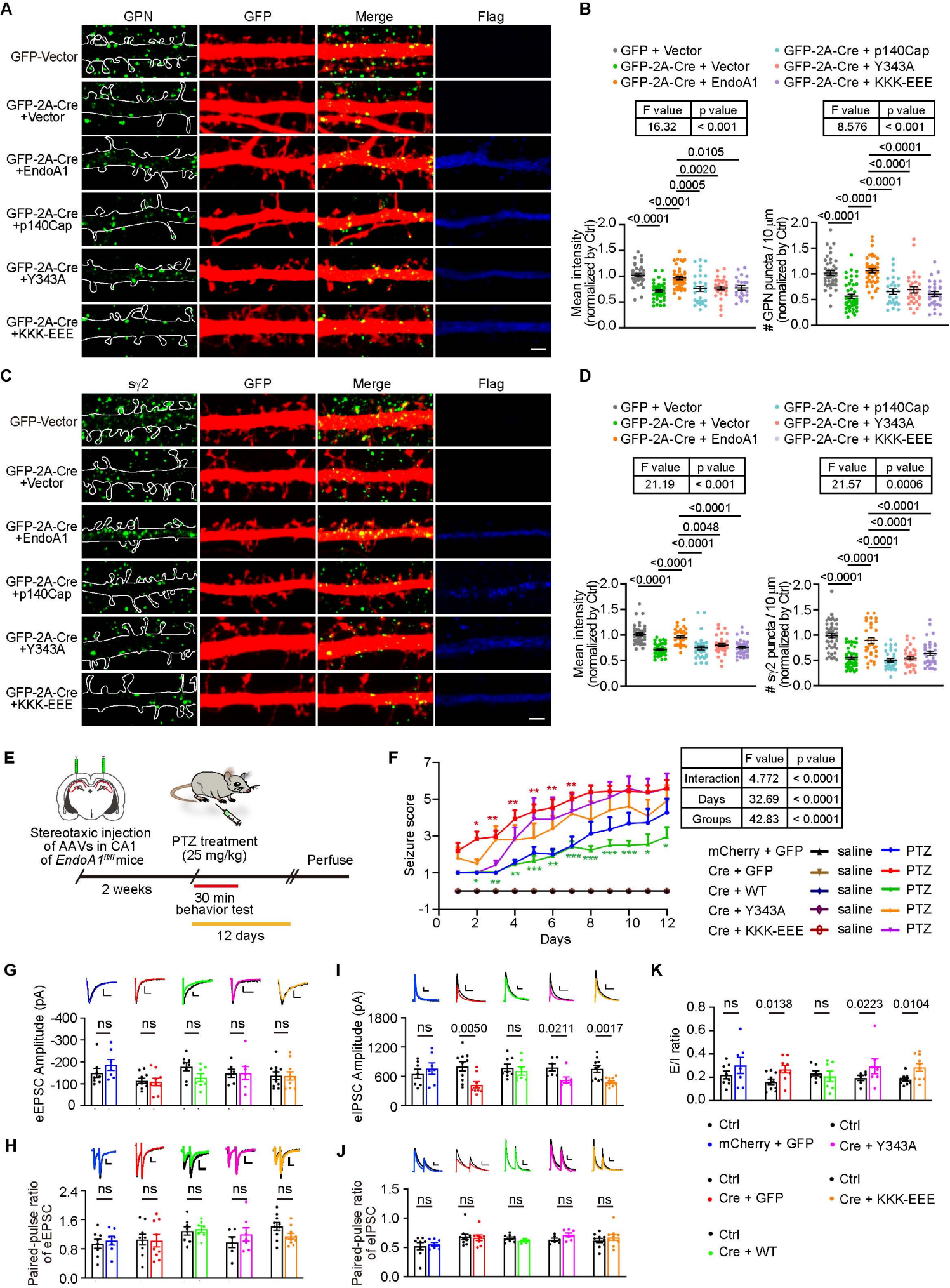
A
GPN
GFP
Merge
Flag
GFP-Vector
GFP-2A-Cre +Vector
GFP-2A-Cre +EndoA1
GFP-2A-Cre +p140Cap
GFP-2A-Cre +Y343A
GFP-2A-Cre +KKK-EEE
B
GFP + Vector
GFP-2A-Cre + Vector
GFP-2A-Cre + EndoA1
GFP-2A-Cre + p140Cap
GFP-2A-Cre + Y343A
GFP-2A-Cre + KKK-EEE
F value | p value
16.32 | < 0.001
8.576 | < 0.001
Mean intensity (normalized by Ctrl)
GPN puncta / 10 μm (normalized by Ctrl)
C
sγ2
GFP
Merge
Flag
D
F value | p value
21.19 | < 0.001
21.57 | 0.0006
Mean intensity (normalized by Ctrl)
sγ2 puncta / 10 μm (normalized by Ctrl)
E
Stereotaxic injection of AAVs in CA1 of EndoA1fl/fl mice
PTZ treatment (25 mg/kg)
Perfuse
2 weeks
30 min behavior test
12 days
F
Seizure score
Days
Interaction | 4.772 | < 0.0001
Days | 32.69 | < 0.0001
Groups | 42.83 | < 0.0001
mCherry + GFP saline PTZ
Cre + GFP saline PTZ
Cre + WT saline PTZ
Cre + Y343A saline PTZ
Cre + KKK-EEE saline PTZ
G
eEPSC Amplitude (pA)
H
Paired-pulse ratio of eEPSC
I
eIPSC Amplitude (pA)
J
Paired-pulse ratio of eIPSC
K
E/I ratio
Ctrl
mCherry + GFP
Cre + GFP
Cre + WT
Cre + Y343A
Cre + KKK-EEE

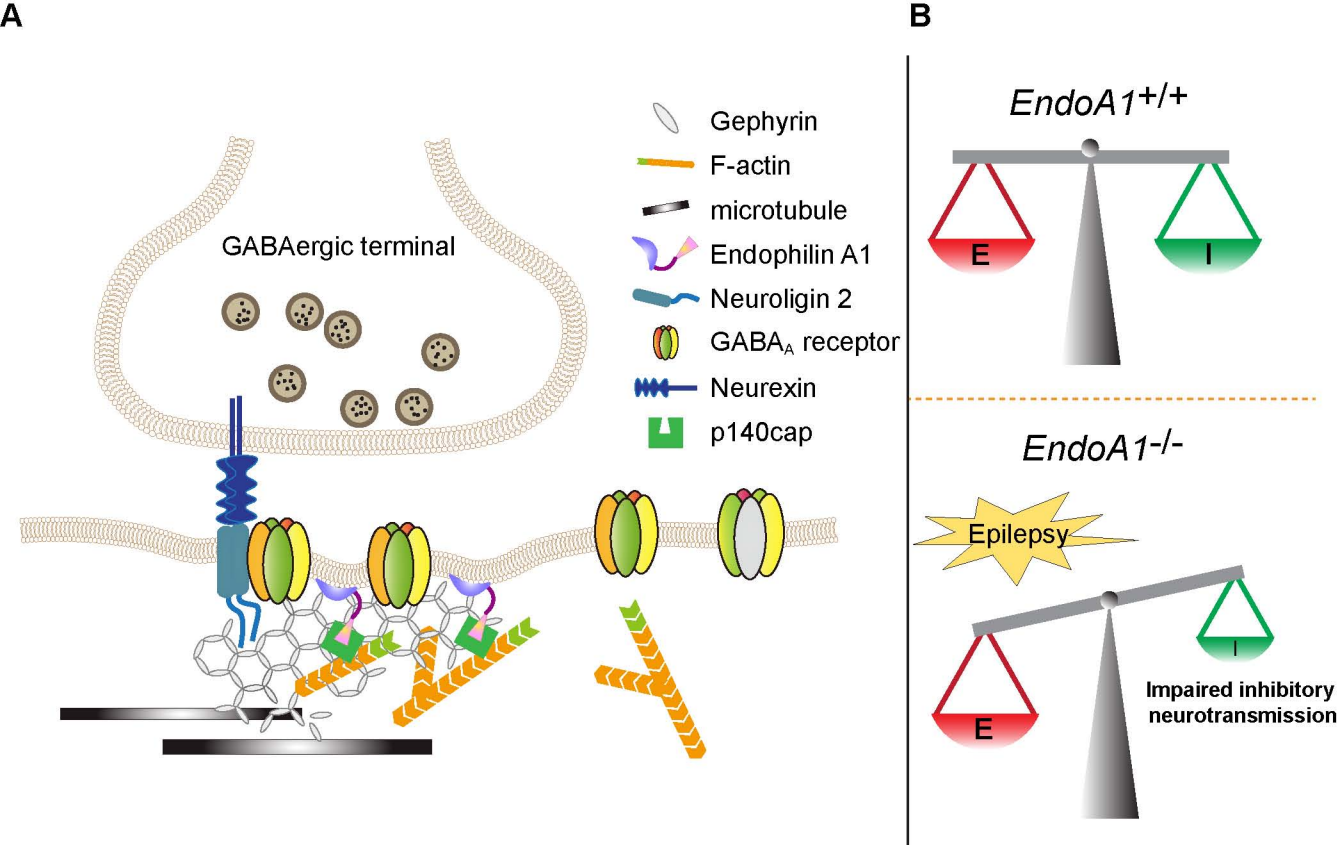
A
GABAergic terminal
Gephyrin
F-actin
microtubule
Endophilin A1
Neuroligin 2
GABA$_A$ receptor
Neurexin
p140cap
B
EndoA1$^{+/+}$
E
I
EndoA1$^{-/-}$
Epilepsy
E
I
Impaired inhibitory neurotransmission

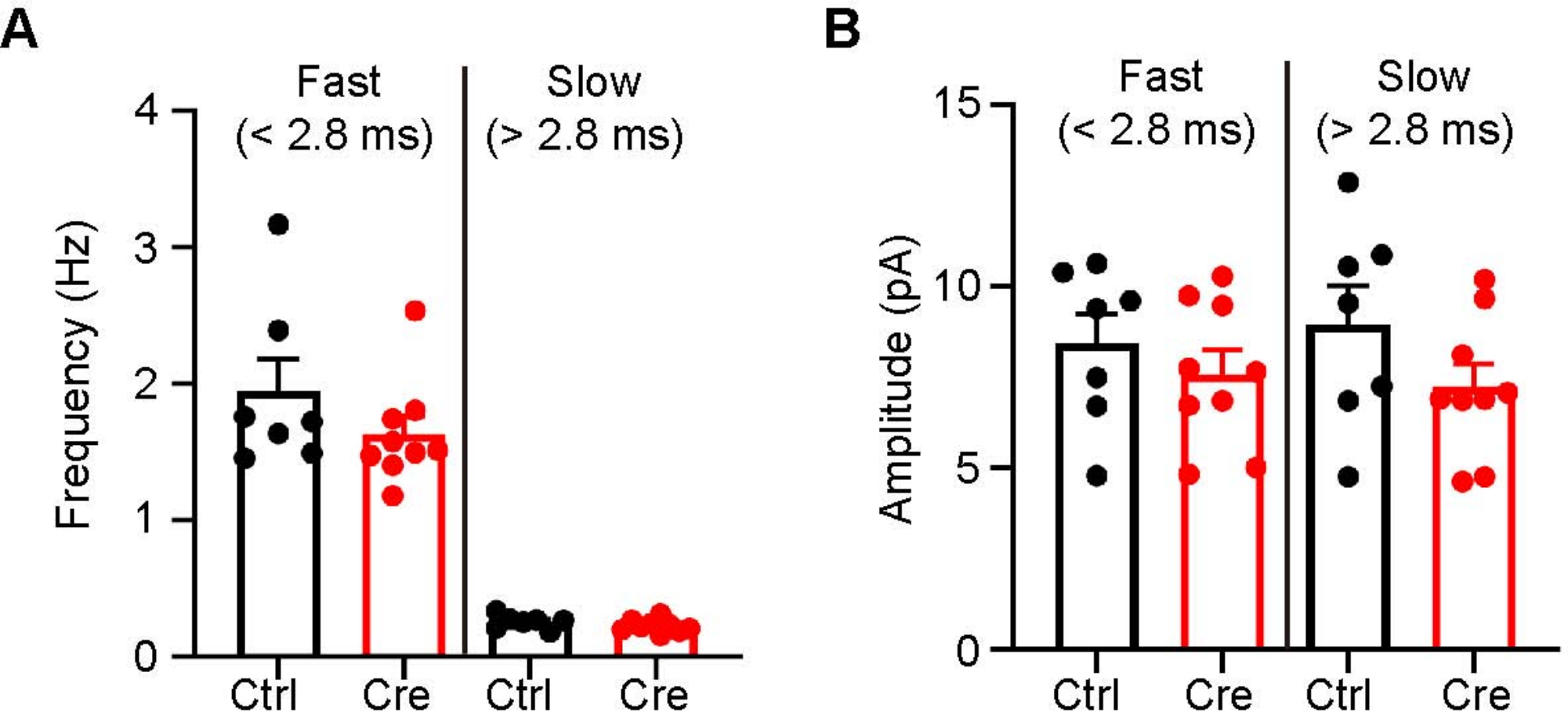
A
Fast
(< 2.8 ms)
Slow
(> 2.8 ms)
Frequency (Hz)
4
3
2
1
0
Ctrl
Cre
Ctrl
Cre
B
Fast
(< 2.8 ms)
Slow
(> 2.8 ms)
Amplitude (pA)
15
10
5
0
Ctrl
Cre
Ctrl
Cre

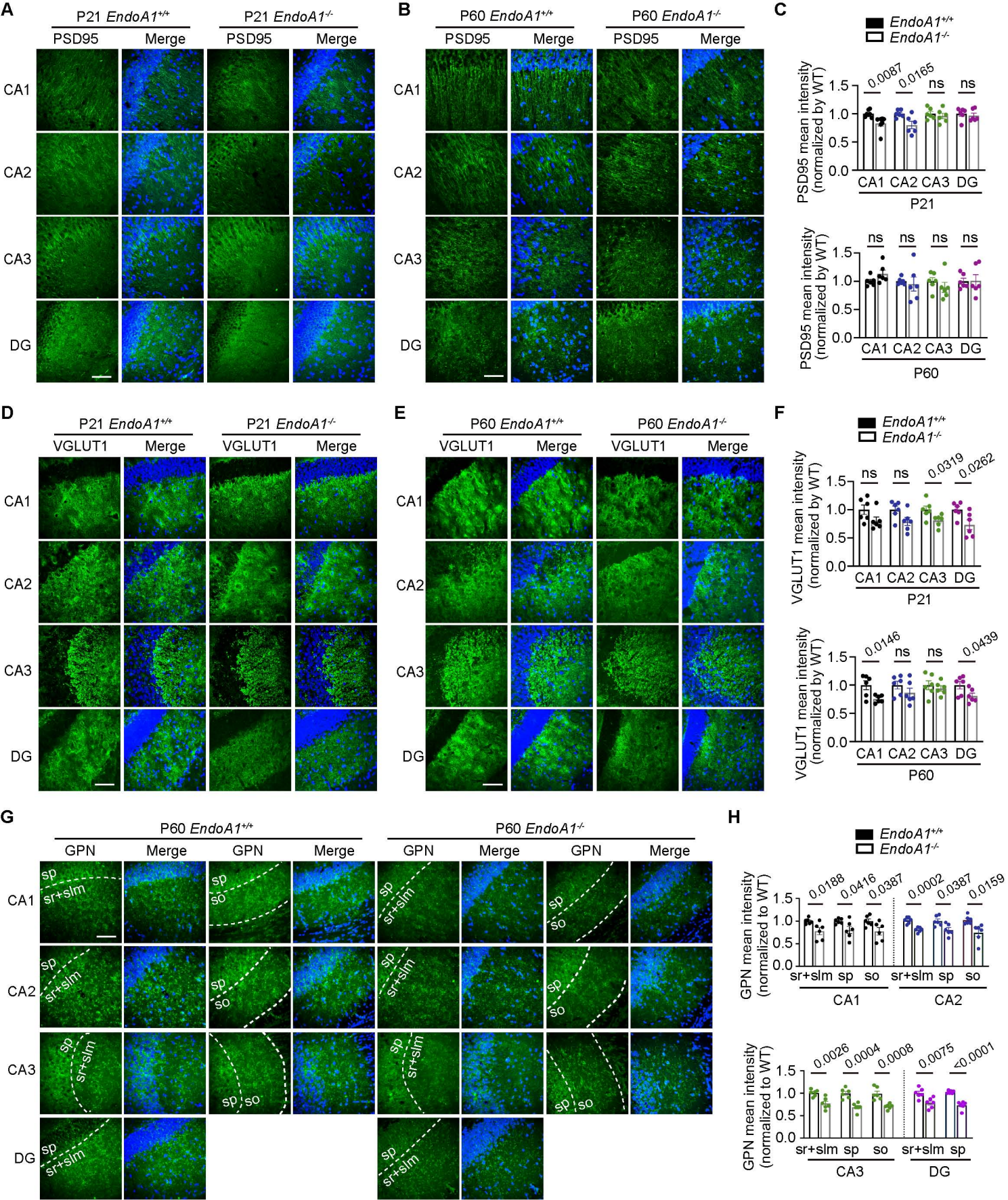
A
P21 EndoA1+/+
P21 EndoA1-/-
PSD95
Merge
CA1
CA2
CA3
DG
B
P60 EndoA1+/+
P60 EndoA1-/-
C
EndoA1+/+
EndoA1-/-
PSD95 mean intensity (normalized by WT)
0.0087
0.0165
ns
P21
P60
D
VGLUT1
E
F
VGLUT1 mean intensity (normalized by WT)
0.0319
0.0262
0.0146
0.0439
G
GPN
sp
sr+slm
so
H
GPN mean intensity (normalized to WT)
0.0188
0.0416
0.0387
0.0002
0.0387
0.0159
0.0026
0.0004
0.0008
0.0075
<0.0001
CA1
CA2
CA3
DG

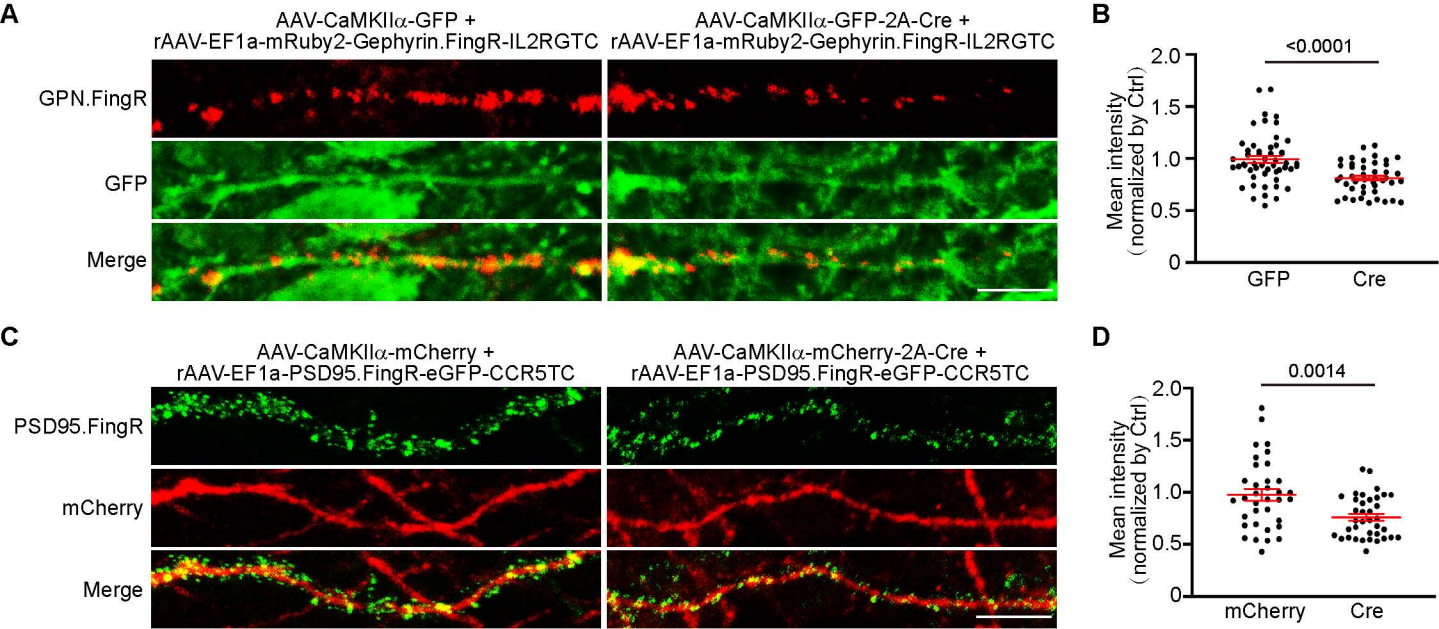
A
AAV-CaMKIIα-GFP +
rAAV-EF1a-mRuby2-Gephyrin.FingR-IL2RGTC
AAV-CaMKIIα-GFP-2A-Cre +
rAAV-EF1a-mRuby2-Gephyrin.FingR-IL2RGTC
GPN.FingR
GFP
Merge
B
<0.0001
Mean intensity
(normalized by Ctrl)
2.0
1.5
1.0
0.5
0
GFP
Cre
C
AAV-CaMKIIα-mCherry +
rAAV-EF1a-PSD95.FingR-eGFP-CCR5TC
AAV-CaMKIIα-mCherry-2A-Cre +
rAAV-EF1a-PSD95.FingR-eGFP-CCR5TC
PSD95.FingR
mCherry
Merge
D
0.0014
Mean intensity
(normalized by Ctrl)
2.0
1.5
1.0
0.5
0
mCherry
Cre

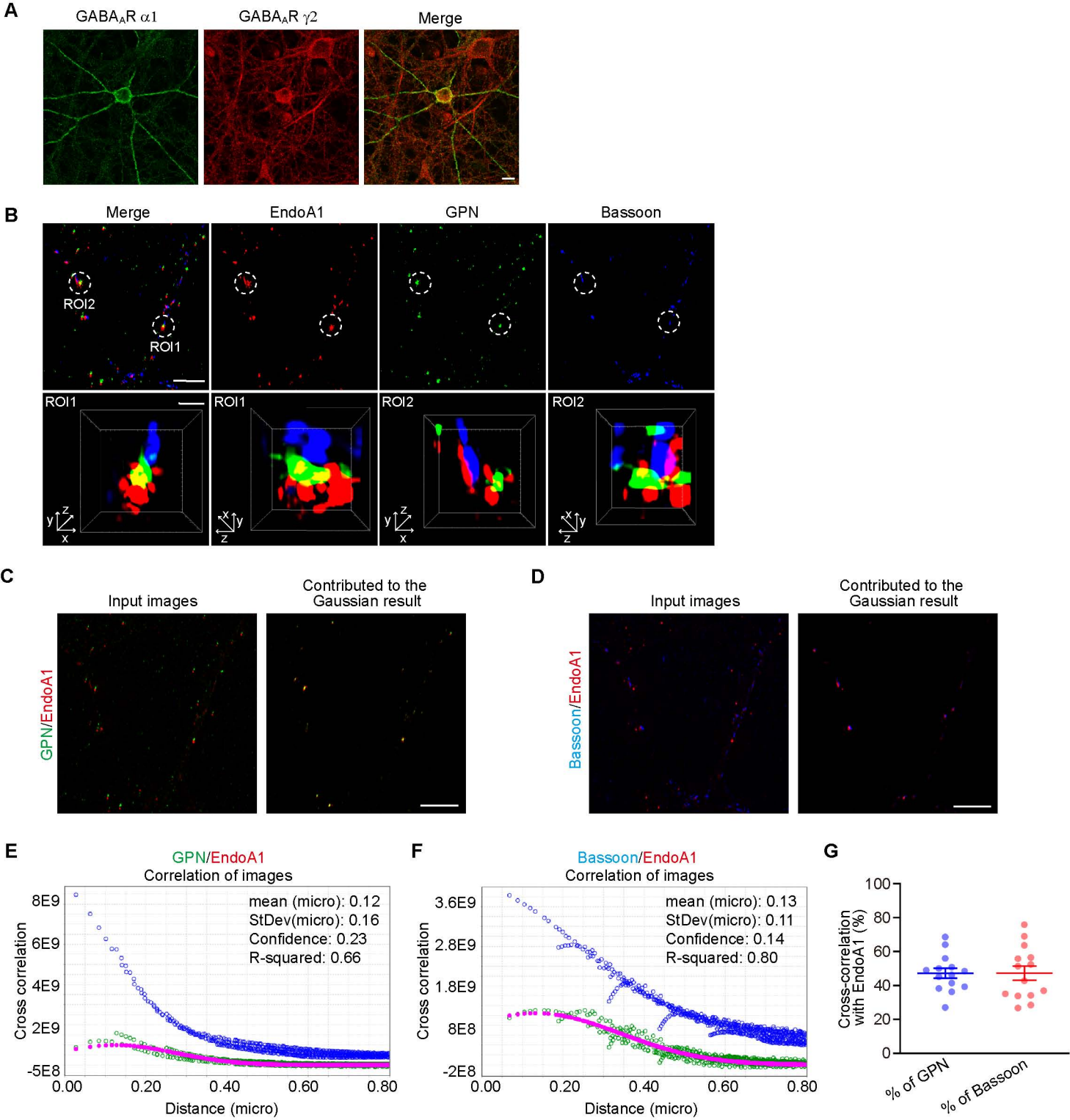
A
GABA$_A$R α1
GABA$_A$R γ2
Merge
B
Merge
EndoA1
GPN
Bassoon
ROI2
ROI1
ROI1
ROI1
ROI2
ROI2
C
Input images
Contributed to the Gaussian result
GPN/EndoA1
D
Input images
Contributed to the Gaussian result
Bassoon/EndoA1
E
GPN/EndoA1
Correlation of images
mean (micro): 0.12
StDev(micro): 0.16
Confidence: 0.23
R-squared: 0.66
Cross correlation
8E9
6E9
4E9
2E9
-5E8
0.00
0.20
0.40
0.60
0.80
Distance (micro)
F
Bassoon/EndoA1
Correlation of images
mean (micro): 0.13
StDev(micro): 0.11
Confidence: 0.14
R-squared: 0.80
Cross correlation
3.6E9
2.8E9
1.8E9
8E8
-2E8
0.00
0.20
0.40
0.60
0.80
Distance (micro)
G
Cross-correlation with EndoA1 (%)
100
80
60
40
20
0
% of GPN
% of Bassoon

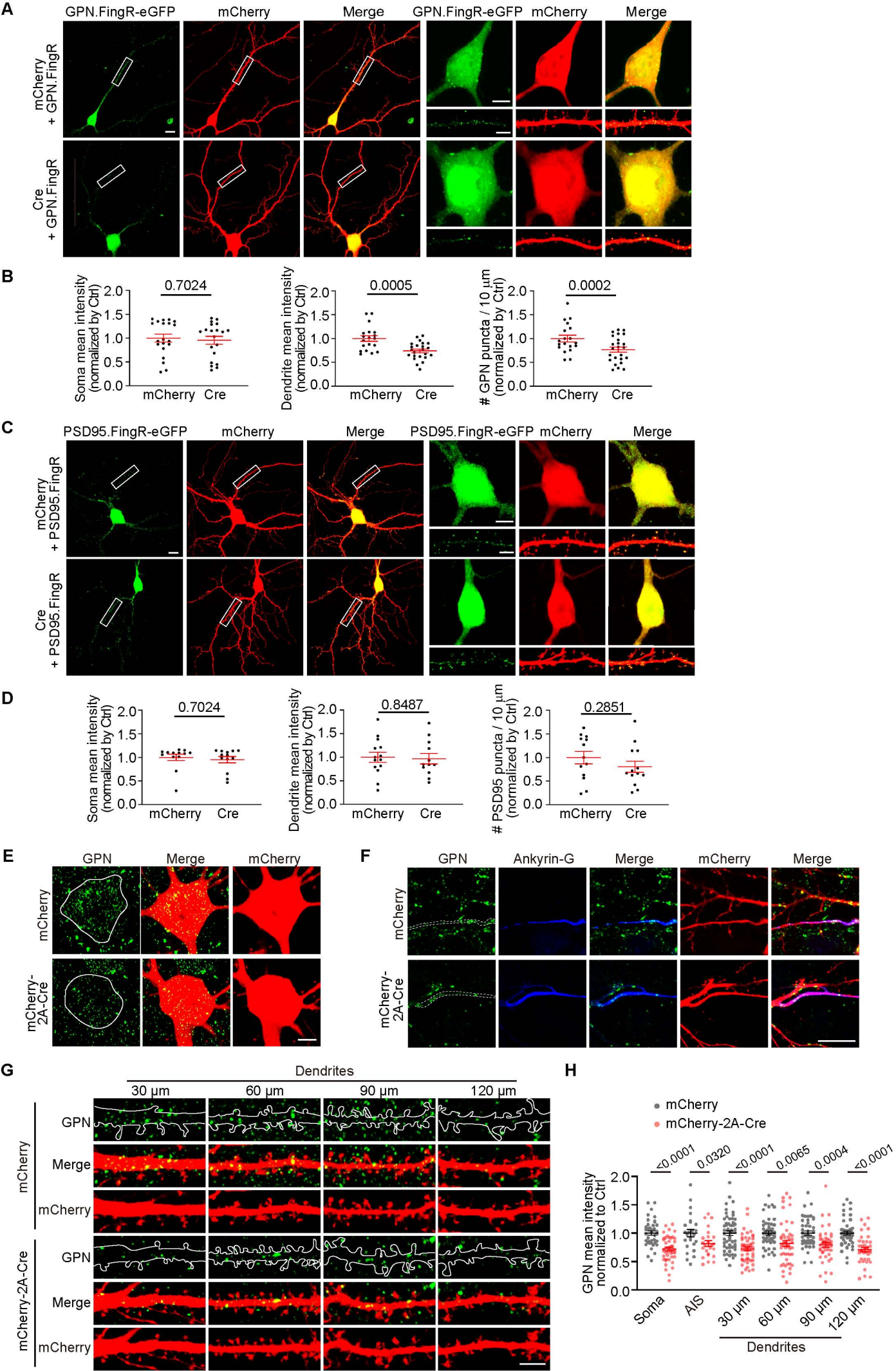
A
GPN.FingR-eGFP
mCherry
Merge
GPN.FingR-eGFP
mCherry
Merge
mCherry + GPN.FingR
Cre + GPN.FingR
B
Soma mean intensity (normalized by Ctrl)
0.7024
Dendrite mean intensity (normalized by Ctrl)
0.0005
GPN puncta / 10 µm (normalized by Ctrl)
0.0002
mCherry
Cre
C
PSD95.FingR-eGFP
mCherry
Merge
PSD95.FingR-eGFP
mCherry
Merge
mCherry + PSD95.FingR
Cre + PSD95.FingR
D
Soma mean intensity (normalized by Ctrl)
0.7024
Dendrite mean intensity (normalized by Ctrl)
0.8487
PSD95 puncta / 10 µm (normalized by Ctrl)
0.2851
mCherry
Cre
E
GPN
Merge
mCherry
mCherry
mCherry-2A-Cre
F
GPN
Ankyrin-G
Merge
mCherry
Merge
mCherry
mCherry-2A-Cre
G
Dendrites
30 µm
60 µm
90 µm
120 µm
mCherry
GPN
Merge
mCherry
mCherry-2A-Cre
GPN
Merge
mCherry
H
mCherry
mCherry-2A-Cre
<0.0001
0.0320
<0.0001
0.0065
0.0004
<0.0001
GPN mean intensity normalized to Ctrl
Soma
AIS
30 µm
60 µm
90 µm
120 µm
Dendrites

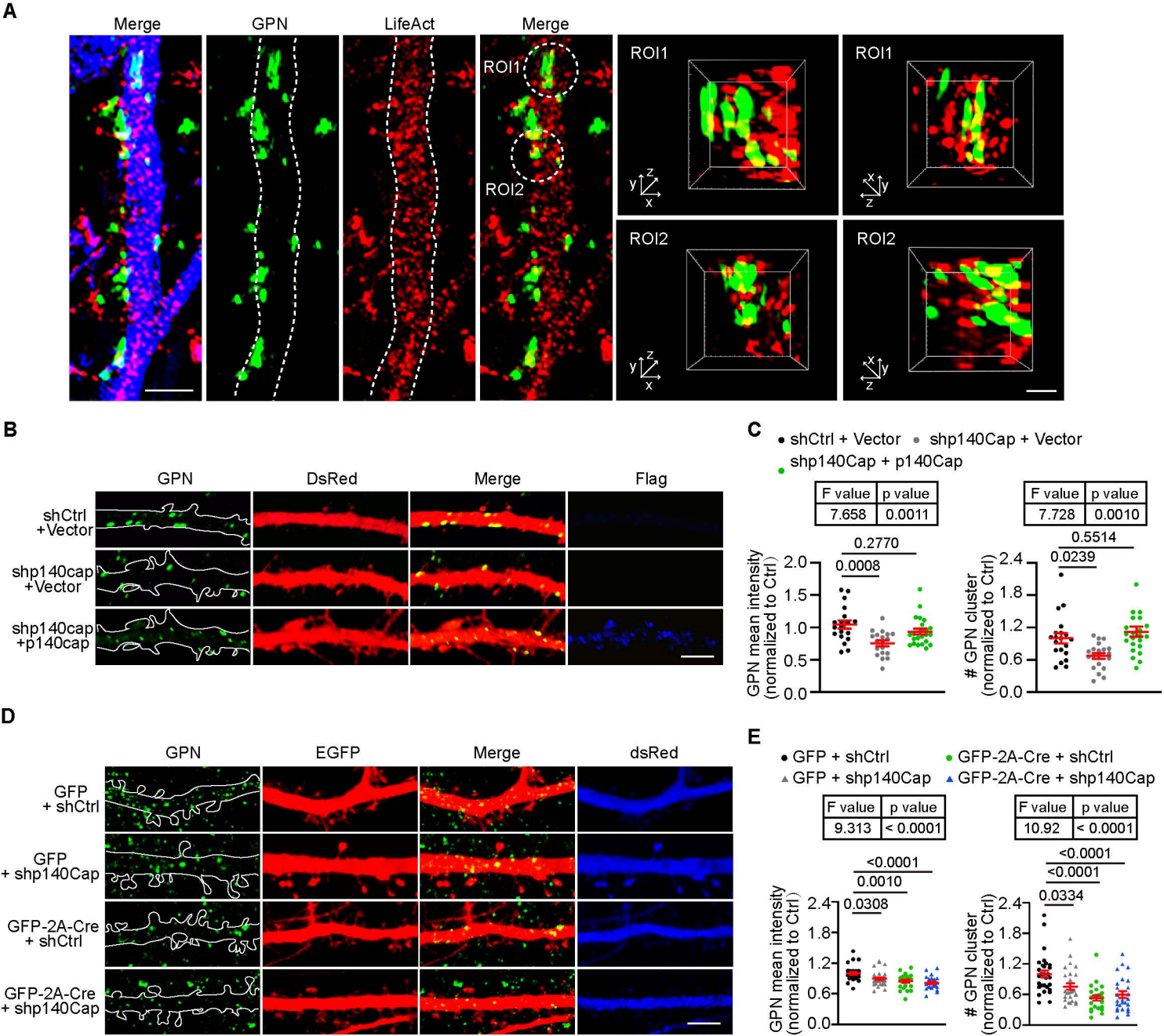
A
Merge
GPN
LifeAct
Merge
ROI1
ROI2
ROI1
ROI1
ROI2
ROI2
B
GPN
DsRed
Merge
Flag
shCtrl +Vector
shp140cap +Vector
shp140cap +p140cap
C
shCtrl + Vector
shp140Cap + Vector
shp140Cap + p140Cap
F value | p value
7.658 | 0.0011
F value | p value
7.728 | 0.0010
0.2770
0.0008
0.5514
0.0239
GPN mean intensity (normalized to Ctrl)
GPN cluster (normalized to Ctrl)
D
GPN
EGFP
Merge
dsRed
GFP + shCtrl
GFP + shp140Cap
GFP-2A-Cre + shCtrl
GFP-2A-Cre + shp140Cap
E
GFP + shCtrl
GFP + shp140Cap
GFP-2A-Cre + shCtrl
GFP-2A-Cre + shp140Cap
F value | p value
9.313 | < 0.0001
F value | p value
10.92 | < 0.0001
<0.0001
0.0010
0.0308
<0.0001
<0.0001
0.0334
GPN mean intensity (normalized to Ctrl)
GPN cluster (normalized to Ctrl)